Unsteady natural convection on an evenly heated vertical plate for Prandtl number Pr < 1

Wenxian Lin[1,2,*] and S. W. Armfield[2]

[1]*Solar Energy Research Institute, Yunnan Normal University, Kunming, Yunnan 650092, People's Republic of China*
[2]*School of Aerospace, Mechanical and Mechatronic Engineering, University of Sydney, NSW 2006, Australia*
(Received 23 May 2005; revised manuscript received 30 September 2005; published 21 December 2005)

The transient behavior of the natural convection boundary-layer flow adjacent to a vertical plate heated with a uniform flux in a quiescent homogeneous ambient fluid with Prandtl number Pr < 1 is investigated by scaling analysis and direct numerical simulation (DNS). The flow is characterized by a startup stage, a short transitional stage and a steady state. The flow is parametrized by the thermal and velocity boundary-layer thickness scales, the vertical velocity scale, the time scale for the boundary layer to reach the steady state and the plate temperature scale. Scaling analysis is used to obtain laws relating these quantities to the flow governing parameters, the Rayleigh number Ra, the Prandtl number, and the Boussinesq number Bo=RaPr which is a much more important control parameter than Ra for small Pr fluids. A series of DNS with selected values of Ra and Pr in the ranges of $10^6 \leqslant Ra \leqslant 10^{10}$ and $0.01 \leqslant Pr \leqslant 0.5$ are used to validate the scaling laws and obtain scaling constants.

I. INTRODUCTION

The transient response of a fluid via an unsteady natural convection flow to a suddenly imposed surface heating condition has been extensively explored in the literatures (see, e.g., Refs. [1–5]). The natural convection flow of fluid with low Prandtl number (Pr < 1) has also received considerable attention due to its large coefficient of heat conduction which is important to practical applications, such as in nuclear reactors where liquid metals with Pr ≪ 1 have been widely used for the rapid cooling purpose and its fundamental importance to fluid mechanics and heat transfer subjects (see, e.g., Refs. [6,7]).

The analytical methods employed previously to solve the natural convection flow of fluid with low Prandtl number may be divided into four types. The first type obtains the numerical solution of a set of ordinary differential equations derived from the original governing partial differential equations via a similarity transformation (see, e.g., Refs. [8]). To obtain the Prandtl number variation using this approach a separate integration of the differential equations has to be performed for each Prandtl number, and hence the results have to be tabulated instead of being represented in a single formula. Furthermore, as pointed out by Kuiken [9], this approach has another disadvantage, that for low Prandtl number the equations contain coefficients of different orders of magnitudes which greatly affects the velocity profiles and causes numerical difficulty for very small Pr. The second approach is to integrate the original partial differential governing equations by means of the integral method of Kármán-Pohlhausen (see, e.g. Refs. [2,10]) which has the advantage that it gives results which display the Prandtl number explicitly. The disadvantage of this is its inaccuracy and its inherent systematic errors [9]. To overcome the short-

comings but to maintain the advantages of the above-mentioned methods, i.e., accuracy and explicit Prandtl number, Kuiken [9] developed the third approach which employs a singular perturbation technique [11]. Additionally, this approach reveals much of the structure of a natural-convection boundary layer at low Prandtl number, as the method of matched asymptotic expansions employed in the approach exposes the predominant factors in different parts of the boundary layer. This approach has been used by many authors for the natural convection flow at low Prandtl number. For example, Park and Carey [12] combined this matched asymptotic expansion technique with an explicit finite-difference scheme to investigate the transient natural convection flow near a vertical surface at low Prandtl number; Joshi [13] used the technique to explore the wall plume at extreme Prandtl numbers and found that transport in a wall plume, which is natural convection flow arising from a line thermal source at the leading edge of a vertical surface, at asymptotically large and small Prandtl numbers exhibits differences from vertical surfaces and the line plume; Merkin *et al.* [14] used the technique to obtain similarity solutions for both the free convection at low Prandtl number on a heated vertical plate with a prescribed power-law heating and the mixed convection at low Prandtl number on a vertical surface with a prescribed heat flux; Ramanaiah and Malarvizhi [15] used the approach for the natural convection adjacent to a vertical plate with three thermal boundary conditions, i.e., the plate is subjected to a prescribed temperature, a prescribed heat flux or a prescribed heat transfer coefficient; Merkin *et al.* [16] also extended this approach to the natural-convection boundary-layer flow on a vertical surface with newtonian heating in which the heat transfer from the surface is proportional to the local surface temperature and to the boundary-layer analysis of the thermal bar which is a descending plane plume of fluid at the temperature of maximum density; Park and Hyun [17] extended the method to the transient buoyancy layer for an infinite vertical wall, where it was shown that the character of the transient layer has a strong dependence on the Prandtl number, which is in contrast to the case

─────────
*Electronic address: wenxian.lin@aeromech.usyd.edu.au; FAX: +61-2-9351-7060

of the steady-state layer, and to the analysis of the transient adjustment processes of an initially stationary and stably stratified fluid in a square container with highly conducting boundary walls; Chamkha [18] used the method to investigate the laminar hydromagnetic natural convection flow along a heated vertical surface in a stratified environment with internal heat absorption.

The fourth approach is to obtain, via scaling analysis, the various scaling laws describing the predominant flow behavior, and to carry out direct numerical simulation (DNS) of the original partial differential governing equations of flow to verify and quantify the scaling laws for the specifically-selected ranges of the flow control parameters, such as the Prandtl number (Pr), the Rayleigh number (Ra), etc. This approach was pioneered by Patterson and Imberger [19] in the study of the transient behavior of unsteady natural convection flow that occurs when the opposing two vertical side-walls of a two-dimensional rectangular cavity are impulsively heated and cooled by an equal amount, and has since become a widely used technique for natural convection flows. For example, this method was used extensively by Bejan [4] to investigate a series of unsteady and steady natural convection flows including forced convection boundary layers, forced convection wakes and natural convection boundary layers, and was strongly recommended for other convection flows and heat transfer processes such as those in porous media [20]; Jannot and Kunc [21] employed such an approach to explore the onset of transition to turbulence in natural convection with gas along a vertical isotherm plane; Kim and Hyun [22] dealt with the convective process of a differentially heated cavity system in response to abrupt imposition of gravity from the quiescent null-gravity initial state by a scaling analysis and direct numerical simulations and obtained the scaling laws describing the small-time, intermediate-time and steady state approaching behavior of the flow; Lin and Armfield [23,24] employed such techniques for the transient processes of cooling an initially homogeneous fluid with $Pr \geqslant 1$ by natural convection in a vertical circular cylinder and in a rectangular container; Lin, Armfield, and Morgan [25] used the same techniques to obtain the scaling laws for the boundary layer development along a vertical isothermal plate in a linearly stratified fluid with $Pr > 1$; Lei and Patterson [26] extended the scaling analysis of [19] to the unsteady natural convection in a triangular enclosure induced by absorption of radiation.

Some other techniques have also been used to investigate natural convection flow at low Prandtl numbers. For example, experimental heat transfer correlations were determined by Humphreys and Welty [27] for natural convection in mercury in a uniformly heated vertical channel during unstable laminar and transitional flow; Bejan and Lage [28] explored the Prandtl number effect on the transition in natural convection along a vertical surface; The two- and three-dimensional numerical simulations of the transition to oscillatory convection in low-Prandtl-number fluids were carried out by Henry *et al.* [29]; Sammouda, Belghith, and Surry [7] used finite element simulation to investigate the transient natural convection of low-Prandtl-number fluids in heated cavity; A linear stability analysis was applied by Sundström and Vynnycky [30] to a family of natural convection flows in

an arbitrarily inclined rectangular enclosure where the flow is driven by prescribed heat or mass fluxes along two opposing walls; The three-dimensional axisymmetry-breaking instability of an axisymmetric convection flow associated with crystal growth from bulk of melt was presented by Gelfgat, Bar-Yoseph and Solan [31]; The low-Prandtl number natural convection in volumetrically heated rectangular enclosures with different aspect ratios was explored by direct numerical two-dimensional simulation by Piazza, Ciofalo, and Arcidiacono [32]. Shapiro and Fedorovich [33] obtained the exact solutions and the Prandtl number dependence of the unsteady natural convection along a vertical plate immersed in a stably stratified fluid induced by an impulsive (step) change in plate temperature, a sudden application of a plate heat flux, and arbitrary temporal variation in plate temperature or plate heat flux by the method of Laplace transforms and a regular perturbation expansion, but focused on the one-dimensional transient natural convection in regions where the leading-edge effect has not yet propagated and for times prior to the onset of any instabilities.

The steady-state behavior of the natural convection boundary-layer flow of an initially quiescent homogeneous Newtonian fluid with $Pr < 1$ adjacent to a vertical plate heated with a uniform flux was investigated by Sparrow and Gregg [8], as mentioned above and as will be detailed in Sec. III C, who obtained a similarity solution for the temperature and velocity distributions, requiring the numerical solution of a set of ordinary differential equations. For small Pr fluids they only calculated the flow behavior at $Pr = 0.1$ due to computing limitations. Scaling laws characterizing the steady-state behavior of this small Pr fluid flow were obtained by Bejan [4] using scaling analysis. However, they have not been verified and quantified. Furthermore, no scaling laws have been developed for the transient behavior of such a flow associated with start-up, which motivates the current work. In the current study, various scaling laws will be developed for the transient behavior of the unsteady natural convection boundary-layer flow of an initially quiescent homogeneous Newtonian fluid with $Pr < 1$ adjacent to a vertical plate heated with a uniform flux by extending the work of Patterson and Imberger [19] and Bejan [4]. The steady-state flow behavior will also be included in the analysis and the resulting steady-state scaling laws will be benchmarked by the similarity solution obtained by Sparrow and Gregg [8], with, as will be shown in Sec. IV, good agreement. Furthermore, a series of DNS with selected values of Ra and Pr in the ranges of $10^6 \leqslant Ra \leqslant 10^{10}$ and $0.01 \leqslant Pr \leqslant 0.5$ will be carried out to verify and quantify various scaling laws obtained from the scaling analysis.

The remaining part of this paper is organized as follows. The scaling analysis will be carried out in Sec. II to develop scaling laws for the parameters characterizing the behavior at different stages of flow development. The numerical methods and the numerical accuracy tests will be described in Sec. III. The scaling laws are then verified and quantified in Sec. IV by a series of DNS results with selected values of Ra and Pr in the ranges of $10^6 \leqslant Ra \leqslant 10^{10}$ and $0.01 \leqslant Pr \leqslant 0.5$. The similarity of the temperature and velocity profiles at different stages of flow development will also be discussed in Sec. IV. Finally, conclusions are presented in Sec. V.

II. SCALING ANALYSIS

Under consideration is the transient behavior of unsteady natural convection boundary-layer flow of an initially quiescent homogeneous Newtonian fluid with Pr < 1 adjacent to a vertical plate heated with a uniform heat flux. The plate of length H lies at $X=0$, and the origin is at $Y=0$, where X and Y are respectively the horizontal and vertical coordinates. It is assumed that the plate boundary conditions are zero velocity and constant T_X^0, where T_X^0 is the temperature gradient at the plate. The ambient fluid is initially at rest and at the temperature T_0. The gravity acts in the negative Y direction. It is further assumed that the flow is laminar and two-dimensional.

The governing equations of motion are the Navier-Stokes equations expressed in two-dimensional incompressible form with the Boussinesq approximation for buoyancy, which together with the temperature transport equation are as follows,

$$U_t + UU_X + VU_Y = -\frac{1}{\rho}P_X + \nu(U_{XX} + U_{YY}) \tag{1}$$

$$V_t + UV_X + VV_Y = -\frac{1}{\rho}P_Y + \nu(V_{XX} + V_{YY}) + g\beta(T - T_0) \tag{2}$$

$$U_X + V_Y = 0, \tag{3}$$

$$T_t + UT_X + VT_Y = \kappa(T_{XX} + T_{YY}) \tag{4}$$

where U and V are the velocity components in the X and Y directions, t is the time, P is the pressure, T is the temperature, β, κ, and ν are the coefficient of thermal expansion, thermal conductivity, and kinematic viscosity of the fluid, respectively and g is the acceleration due to gravity.

After the initiation of the flow, a vertical boundary layer will be developed adjacent to the plate. The boundary layer will experience a start-up stage, followed by a short transitional stage before reaching a steady state, as illustrated in Fig. 1, where the parameters characterizing the flow behavior at these stages, i.e., the plate temperature scale T_w, the thermal boundary-layer thickness scale Δ_T, the inner and outer velocity boundary-layer thicknesses Δ_{vi} and Δ_{vo}, the vertical velocity scale V_m within the boundary layer, and the time scale t_s for the boundary layer to reach the steady state, are defined (it should be noted that although all these parameters reach the steady state at the same time scale t_s, numerically it will be much easier to determine the individual time scales at the moment when each individual parameter reaches its maximum value, as illustrated in the figure. It is expected that all these time scales will have the same scaling law, although the individual constants of proportionality will be a bit different from each other, as will be shown in Sec. IV). A further illustration and definition of the start-up stage and the steady-state stage of the boundary-layer development and the parameters describing the flow behavior at these development stages are sketched in Fig. 2. Scaling laws will be developed in the subsequent scaling analysis for these parameters at both the start-up stage and the steady-state stage.
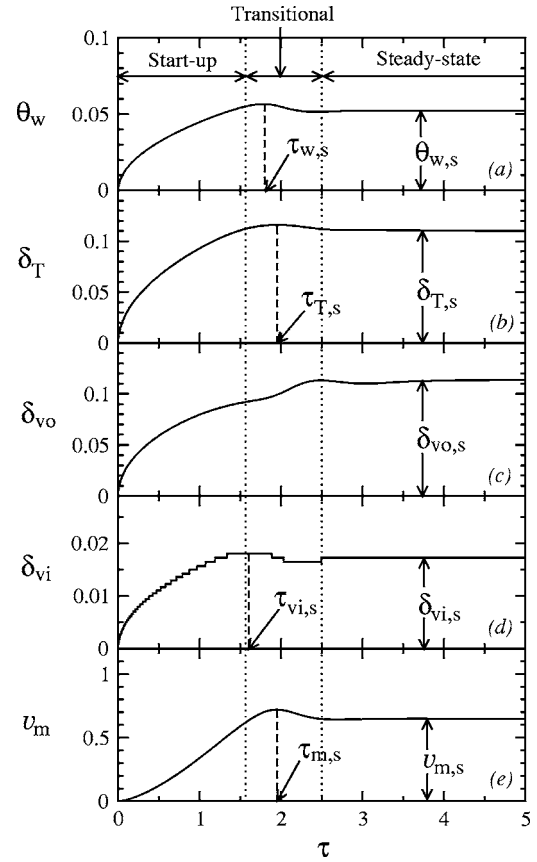

FIG. 1. A definition of the three distinct stages of the boundary-layer development and the numerically simulated typical time series of (a) the plate temperature θ_w ($\theta_w = [T_w - T_0]/[T_x^0 H]$); (b) the thermal boundary-layer thickness δ_T ($\delta_T = \Delta_T/H$); (c) the outer velocity boundary-layer thickness δ_{vo} ($\delta_{v0} = \Delta_{vo}/H$); (d) the inner velocity boundary-layer thickness δ_{vi} ($\delta_{vi} = \Delta_{vi}/H$); (e) the maximum vertical velocity v_m ($v_m = V_m/V_0$) within the boundary layer, respectively, at the height of $Y = 0.5H$ for the specific case of Ra $= 10^8$ and Pr $= 0.1$. τ is made dimensionless by H/V_0, where V_0 is the characteristic velocity defined by Eq. (18).

The start-up stage is dominated by conductive heat transfer in the fluid adjacent to the plate, resulting in a vertical thermal boundary layer of thickness $O(\Delta_T)$ adjacent to the plate, where, from Eq. (4), the balance between the thermal inertia $O(\Delta T/t)$ and the conduction normal to the wall $O(\kappa\Delta T/\Delta_T^2)$ gives

$$\Delta_T \sim \kappa^{1/2}t^{1/2}. \tag{5}$$

The plate temperature scale T_w is then

$$T_w \sim T_X^0\Delta_T \sim T_X^0\kappa^{1/2}t^{1/2}. \tag{6}$$

At the same time, a velocity boundary layer also forms within the thermal boundary layer due to the buoyancy. It is apparent that this velocity boundary layer can be divided into an inner region and an outer region, with the location at which the maximum vertical velocity V_m occurs as the appropriate dividing point. This dividing location, denoted as Δ_{vi}, is the thickness scale of the inner velocity boundary layer.
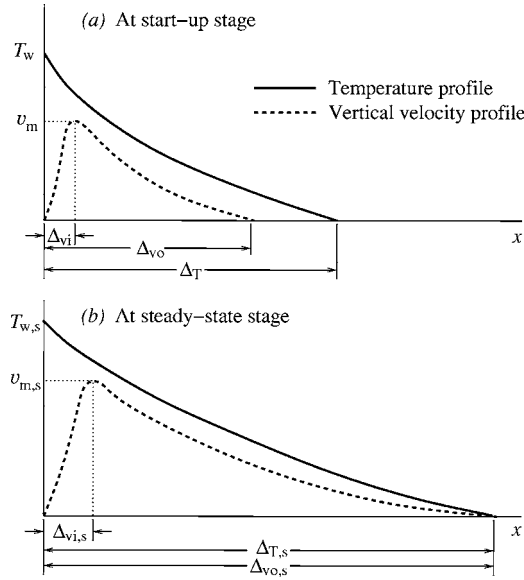
FIG. 2. A sketch of the start-up stage and the steady-state stage of the boundary-layer development and the parameters describing the flow behavior at these development stages.

Within the outer velocity boundary layer, the dominant balance in Eq. (2) is between the inertia $O(\Delta V/t)$, the friction $O(\nu \Delta V/\Delta_T^2)$, and the buoyancy $O(g\beta\Delta T)$ for Pr<1, where $\Delta T = T_X^0 \Delta_T$ is the total temperature variation over the boundary layer, that is,

$$\frac{V_m}{t} \sim \frac{\nu V_m}{\Delta_T^2} \sim g\beta\Delta T. \tag{7}$$

With Eq. (5) this scaling becomes

$$\frac{V_m}{t} \sim \text{Pr}\frac{V_m}{t} \sim g\beta T_X^0 \kappa^{1/2}t^{1/2}, \tag{8}$$

giving

$$V_m \sim \frac{g\beta T_X^0 \kappa^{1/2}t^{3/2}}{O(1) + O(\text{Pr})}. \tag{9}$$

This scaling indicates that for small Pr fluids (Pr<1) the contribution from the friction $O(\nu \Delta V/\Delta_T^2)$ is smaller than that from the inertia $O(\Delta V/t)$ to balance the buoyancy $O(g\beta\Delta T)$ within the outer velocity boundary layer and it becomes negligible when Pr→0.

On the other hand, the dominant balance in Eq. (2) within the inner velocity boundary layer is between the inertia $O(V_m/t)$ and the friction $O(\nu V_m/\Delta_{vi}^2)$, giving

$$\Delta_{vi} \sim \nu^{1/2}t^{1/2} \sim \text{Pr}^{1/2}\Delta_T, \tag{10}$$

which indicates that for small Pr fluids, the inner velocity boundary layer is always within the thermal boundary layer ($\Delta_{vi} < \Delta_T$).

After the start-up stage, the dominant balance in Eq. (4) gradually shifts from that between the thermal inertia $O(\Delta T/t)$ and the conduction $O(\kappa\Delta T/\Delta_T^2)$ to that between the convection $O(V_m\Delta T/Y)$ and the conduction, represented by a

short stage of transition, until the latter balance becomes fully dominant and the development of the thermal boundary layer then reaches the steady state.

At steady state, the balance between the thermal inertia and the convection in Eq. (4) gives

$$\frac{\Delta T}{t} \sim V_m\frac{\Delta T}{Y}, \tag{11}$$

that is

$$V_m \sim \frac{Y}{t}. \tag{12}$$

Using Eqs. (9) and (12), the time scale for the thermal boundary layer to reach the steady state is,

$$t_s \sim [O(1) + O(\text{Pr})]^{2/5}\frac{H^2}{\kappa(\text{RaPr})^{2/5}}\left(\frac{Y}{H}\right)^{2/5}, \tag{13}$$

where $\text{Ra} = g\beta T_X^0 H^4/\nu\kappa$ is the Rayleigh number and Pr $=\nu/\kappa$ is the Prandtl number.

At this time, the thermal boundary layer reaches the steady-state thickness scale $\Delta_{T,s}$, which, from Eq. (5), is as follows,

$$\Delta_{T,s} \sim [O(1) + O(\text{Pr})]^{1/5}\frac{H}{(\text{RaPr})^{1/5}}\left(\frac{Y}{H}\right)^{1/5}, \tag{14}$$

and the vertical velocity within the boundary layer reaches the steady-state scale $V_{m,s}$, which, from Eq. (9), is as follows,

$$V_{m,s} \sim \frac{1}{[O(1) + O(\text{Pr})]^{2/5}}\frac{\kappa(\text{RaPr})^{2/5}}{H}\left(\frac{Y}{H}\right)^{3/5}. \tag{15}$$

The steady-state plate temperature scale $T_{w,s}$ is then obtained from $\Delta_{T,s}$ as

$$T_{w,s} \sim T_X^0\Delta_{T,s} \sim [O(1) + O(\text{Pr})]^{1/5}\frac{T_X^0 H}{(\text{RaPr})^{1/5}}\left(\frac{Y}{H}\right)^{1/5}. \tag{16}$$

The inner velocity boundary layer reaches the steady-state thickness scale Δ_{vi} which, from Eq. (10), is as follows

$$\Delta_{vi,s} \sim [O(1) + O(\text{Pr})]^{1/5}\frac{\text{Pr}^{1/2}H}{(\text{RaPr})^{1/5}}\left(\frac{Y}{H}\right)^{1/5} \sim \text{Pr}^{1/2}\Delta_{T,s}. \tag{17}$$

As illustrated in Figs. 1 and 2, when Pr<1 the outer velocity boundary layer thickness must be as wide as the thermal boundary layer when the boundary-layer development reaches the steady state, and therefore the outer velocity boundary layer thickness scale Δ_{vo} must be the same as the thermal boundary-layer thickness scale Δ_T and all the scaling laws obtained for Δ_T, both at the start-up stage and the steady-state stage, must apply for Δ_{vo}.

An examination of the scaling laws (13)–(17) obtained above reveals that the new parameter group RaPr becomes a dominant parameter characterizing the small Pr fluid flows considered here. In fact, as pointed out by Bejan [4], RaPr, which is called the Boussinesq number (i.e., Bo=RaPr), plays the same role for small Pr fluids as Ra plays for high Pr

fluids and its use is more appropriate than the use of Ra in small Pr fluid flows. In the subsequent sections, we will use Bo instead of Ra.

From Eq. (15), it is obvious that the following velocity scale

$$V_0 = \frac{\kappa(\mathrm{RaPr})^{2/5}}{H} = \frac{\kappa \mathrm{Bo}^{2/5}}{H}, \qquad (18)$$

is the appropriate characteristic velocity scale for the development of the boundary layer with $\mathrm{Pr} < 1$. Using V_0, H, H/V_0, and $T_X^0 H$ as the characteristic velocity, length, time, and temperature for the development of the boundary layer, the scaling laws obtained above can be made dimensionless as follows.

During the start-up stage, the scaling laws (5), (6), (9), and (10) have the following dimensionless forms

$$\delta_T = \frac{\Delta_T}{H} \sim \frac{\tau^{1/2}}{\mathrm{Bo}^{1/5}}, \qquad (19)$$

$$\theta_w = \frac{T_w}{T_X^0 H} \sim \delta_T \sim \frac{\tau^{1/2}}{\mathrm{Bo}^{1/5}}, \qquad (20)$$

$$v_m = \frac{V_m}{V_0} \sim \frac{\tau^{3/2}}{O(1) + O(\mathrm{Pr})}, \qquad (21)$$

$$\delta_{vi} = \frac{\Delta_{vi}}{H} \sim \frac{\mathrm{Pr}^{1/2} \tau^{1/2}}{\mathrm{Bo}^{1/5}} \sim \mathrm{Pr}^{1/2} \delta_T, \qquad (22)$$

where $\tau = t/(H/V_0)$ is the dimensionless time; and at the steady state, the scaling laws (13)–(17) become dimensionless as follows,

$$\tau_s = \frac{t_s}{(H/V_0)} \sim [O(1) + O(\mathrm{Pr})]^{2/5} y^{2/5}, \qquad (23)$$

$$\delta_{T,s} = \frac{\Delta_{T,s}}{H} \sim [O(1) + O(\mathrm{Pr})]^{1/5} \left(\frac{y}{\mathrm{Bo}}\right)^{1/5}, \qquad (24)$$

$$v_{m,s} = \frac{V_{m,s}}{V_0} \sim \frac{y^{3/5}}{[O(1) + O(\mathrm{Pr})]^{2/5}}, \qquad (25)$$

$$\theta_{w,s} = \frac{T_{w,s}}{T_X^0 H} \sim [O(1) + O(\mathrm{Pr})]^{1/5} \left(\frac{y}{\mathrm{Bo}}\right)^{1/5}, \qquad (26)$$

$$\delta_{vi,s} = \frac{\Delta_{vi,s}}{H} \sim \mathrm{Pr}^{1/2}[O(1) + O(\mathrm{Pr})]^{1/5} \left(\frac{y}{\mathrm{Bo}}\right)^{1/5} \sim \mathrm{Pr}^{1/2} \delta_{T,s}, \qquad (27)$$

where $y = Y/H$ is the dimensionless location on the plate.

From these scaling laws, it is seen that the development of the boundary layer at the start-up stage is one-dimensional as it is only τ dependent and is y independent. However, it becomes two-dimensional and y dependent at steady state. It is apparent that this dependence change-over occurs in the transitional stage in which the τ dependence gradually diminishes and the dependence on y gradually increases until
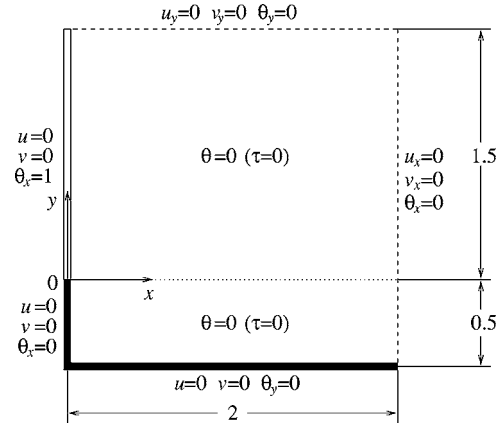

FIG. 3. The computational domain and the initial and boundary conditions for the direct numerical simulations.

at steady state the former disappears and the latter becomes fully dominant.

From Eq. (24), it can also be seen that the existence of a distinct boundary layer, where convection prevails, requires that $\delta_{T,s} \ll 1$, which, in turn, requires $\mathrm{Bo} \gg 1$ as the maximal value of y is one and $[O(1) + O(\mathrm{Pr})]$ is a constant of the order of one for a specific Pr value, as will be shown in Sec. IV. When $\mathrm{Bo} \lesssim 1$, the boundary layer will become indistinguishable and conduction will dominate the flow. As all the scaling laws obtained so far have been developed with the assumption of a distinct convective boundary layer, these scaling laws are therefore only valid for $\mathrm{Bo} \gg 1$. In the subsequent sections, our numerical simulations will also be limited within this distinct convective boundary layer regime.

III. NUMERICAL METHODS AND ACCURACY TEST

A. Governing equations in dimensionless form and the initial and boundary conditions

The governing equations can be recast in non-dimensional form as follows using $V_0 = \kappa \mathrm{Bo}^{2/5}/H$, $T_X^0 H$, H, H/V_0, and ρV_0^2 as the respective characteristic velocity, temperature, length, time, and pressure scales,

$$u_\tau + u u_x + v u_y = -p_x + \frac{\mathrm{Pr}}{\mathrm{Bo}^{2/5}}(u_{xx} + u_{yy}), \qquad (28)$$

$$v_\tau + u v_x + v v_y = -p_y + \frac{\mathrm{Pr}}{\mathrm{Bo}^{2/5}}(v_{xx} + v_{yy}) + \mathrm{Bo}^{1/5}\theta, \quad (29)$$

$$u_x + v_y = 0, \qquad (30)$$

$$\theta_\tau + u\theta_x + v\theta_y = \frac{1}{\mathrm{Bo}^{2/5}}(\theta_{xx} + \theta_{yy}). \qquad (31)$$

To minimize the effect of the boundaries in the direct numerical simulations, the computational domain shown in Fig. 3 is used in the simulations, where an extra region with a dimensionless height of 0.5 and a dimensionless width of

2.0 has been added to both the top and the bottom and the following initial and boundary conditions have been used in the simulations,

$$u = v = 0, \theta = 0 \text{ at all } x, y \text{ when } \tau < 0;$$

and

$$u = v = 0, \theta_x = 0 \text{ at } x = 0, -0.5 \leq y \leq 0;$$

$$u = v = 0, \theta_x = 1 \text{ at } x = 0, 0 \leq y \leq 1.5;$$

$$u_x = v_x = \theta_x = 0 \text{ at } x = 2, -0.5 \leq y \leq 1.5;$$

$$u = v = 0, \theta_y = 0 \text{ at } 0 \leq x \leq 2, y = -0.5;$$

$$u_y = v_y = \theta_y = 0 \text{ at } 0 \leq x \leq 2, y = 1.5 \text{ when } \tau \geq 0.$$

B. Numerical algorithm

The governing equations are discretized on a nonstaggered mesh using finite volumes, with standard second-order central difference schemes used for the viscous, pressure gradient and divergence terms. The QUICK third-order upwind scheme is used for the advective terms [34]. The second-order Adams-Bashforth scheme and Crank-Nicolson scheme are used for the time integration of the advective terms and the diffusive terms, respectively. To enforce the continuity, the pressure correction method is used to construct a Poisson's equation which is solved using the preconditioned GMRES method. Detailed descriptions of these schemes were given in Ref. [35] and the code has been widely used for the simulation of a range of buoyancy dominated flows, including the travelling waves in natural convection in a cavity [36], the vortex generation and shedding from a circular cylinder in oscillatory plus mean flow [37], the internal wave-wave interaction in a stratified fluid [38], founain flows [39], propagating turbulent premixed flames [40], etc.

To ensure that a suitable resolution is maintained in the numerical simulations, a nonuniform computational mesh has been used which concentrates points in the boundary layer and near the boundaries and is relatively coarse in the interior. Specifically, the mesh is constructed using a stretched grid, with nodes concentrated in the region of $x = 0$ and $y = 0$ of the computational domain shown in Fig. 3. The nearest grid point is located 0.0001 from the domain boundaries in the x-direction and 0.0005 from $y = 0$ in the y-direction. Subsequently, the mesh expands at a fixed rate of 3.6% in the x-direction and 2.0% in the y-direction up to $x = y = 0.1$. After that, the mesh size expansion rate decreases at a rate of 10% until it reaches zero, resulting in 284 $\times$ 290 grid points with a constant coarser mesh in the interior of the domain. The time-step used in the simulations is 5×10^{-5}. An extensive mesh and time-step dependency analysis has been carried out to ensure that the solutions are grid-free and accurate. More detailed information about the numerical algorithm can be found in Ref. [23].

TABLE I. DNS results of $\theta_w(y/\text{Bo})^{-1/5}$ and their errors from the similarity value of $\theta_w(y/\text{Bo})^{-1/5} = 1.511$ for different Bo and y in the range of $10^5 \leq \text{Bo} \leq 10^9$ with Pr = 0.1.

Bo	y	$\theta_w(y/\text{Bo})^{-1/5}$	Error
10^5	0.5	1.478	−2.18%
10^6	0.5	1.492	−1.26%
10^7	0.5	1.503	−0.53%
10^8	0.5	1.508	−0.20%
10^9	0.5	1.511	0.00%
10^7	0.1	1.469	−2.78%
10^7	0.3	1.499	−0.79%
10^7	0.7	1.507	−0.26%
10^7	0.9	1.510	−0.07%

C. Numerical accuracy test

Sparrow and Gregg [8] gave the following similarity solution for $\theta_{w,s}$, which is the plate temperature scale at the steady-state stage of its development,

$$\theta_{w,s} = -5^{1/5} \text{Pr}^{2/5} F_\theta(\text{Pr}) \left(\frac{y}{\text{Bo}} \right)^{1/5}, \tag{32}$$

where $F_\theta(\text{Pr})$ is a function of Pr and its value can be obtained by simultaneously solving two ordinary differential equations [the Eqs. (3a) and (3b) subject to the boundary conditions Eq. (11) in Ref. [8]]. For Pr = 0.1, Sparrow and Gregg [8] found that $F_\theta(\text{Pr}) = -2.7507$, which gives the following solution for Pr = 0.1,

$$\theta_{w,s} = 1.511 \left(\frac{y}{\text{Bo}} \right)^{1/5}. \tag{33}$$

It is worthwhile to note that the approximate solution obtained by the von Kármán–Pohlhausen method [8] is

$$\theta_{w,s} = \frac{(360)^{1/5}}{2} (0.8 + \text{Pr})^{1/5} \left(\frac{y}{\text{Bo}} \right)^{1/5} = 1.589 \left(\frac{y}{\text{Bo}} \right)^{1/5}, \tag{34}$$

for Pr = 0.1, which shows an error of 5.16% from the similarity solution given by Eq. (33), and the solution obtained by the perturbation method [14] is

$$\theta_{w,s} = (1.31411 + 0.257 \text{Pr}^{1/2}) \left(\frac{y}{\text{Bo}} \right)^{1/5} = 1.395 \left(\frac{y}{\text{Bo}} \right)^{1/5}, \tag{35}$$

for Pr = 0.1, which shows an error of −7.68% from the similarity solution given by Eq. (33).

The DNS results for $\theta_w/(y/\text{Bo})^{1/5}$ and their errors from the similarity solution given by Eq. (33) are listed in Table I for different Bo and y in the range of $10^5 \leq \text{Bo} \leq 10^9$ with Pr = 0.1. It is found that when Bo $\geq 10^7$ and $y \geq 0.3$ the DNS results are in good agreement with the similarity solutions, with errors of within ±1.00% (notably it is observed that for Bo = 10^9 and $y = 0.5$, the DNS result exactly matches the similarity solution). The larger errors observed for Bo $< 10^7$
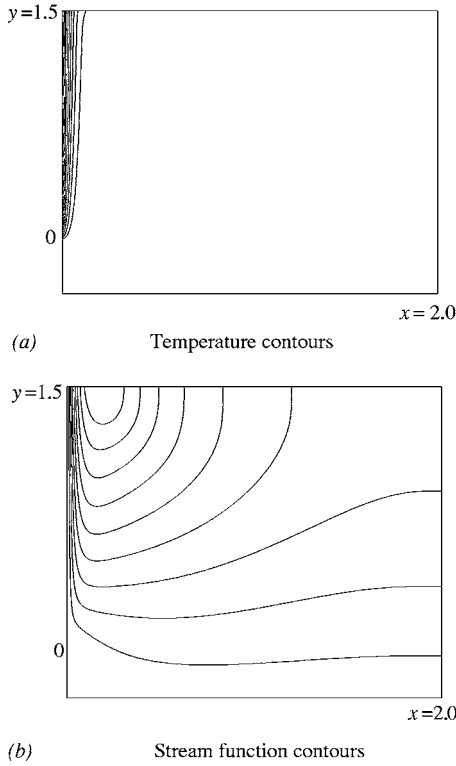
FIG. 4. Numerically obtained typical temperature contours (a) and stream function contours (b) at steady state ($\tau=10$) for Bo$=10^7$ and Pr$=0.1$.

are mainly due to the deviation from the boundary layer assumption made in Ref. [8] which requires Bo$\gg 1$ to ensure $\delta_T \ll 1$. If Bo is taken as the local Boussinesq number, based on plate location y, it is also seen that for small y the similarity solution is expected to be less accurate.

IV. DNS RESULTS

In this section, the scaling laws obtained above will be verified and quantified by a series of DNS with selected values of Bo and Pr in the range of $10^6 \leq$ Bo$/$Pr$\leq 10^{10}$ and $0.01 \leq$ Pr≤ 0.5. A total of 8 DNS runs have been carried out for this purpose, that is, runs 1–5 with Bo$=10^5$, 10^6, 10^7, 10^8, and 10^9 while keeping Pr$=0.1$ unchanged have been carried out to show the dependence of the scaling laws on Bo and runs 6–7, 3 and 8 with Pr$=0.01$, 0.05, 0.1, and 0.5 while keeping Bo$/$Pr$=10^8$ unchanged have been carried out to show the dependence of the scaling laws on Pr.

Figure 4 contains the numerically obtained temperature and stream function contours at steady state for Bo$=10^7$ and Pr$=0.1$. The stream function contours show the basic structure of the flow, with the boundary layer formed adjacent to the heated part of the plate ($y \geq 0$), entraining fluid through the far-field open boundaries and discharging it through the downstream boundary at large y. The temperature contours clearly show the heated region of the $x=0$ boundary, corresponding to the heated plate, and show the increase in width and intensity of the boundary layer with increasing y.
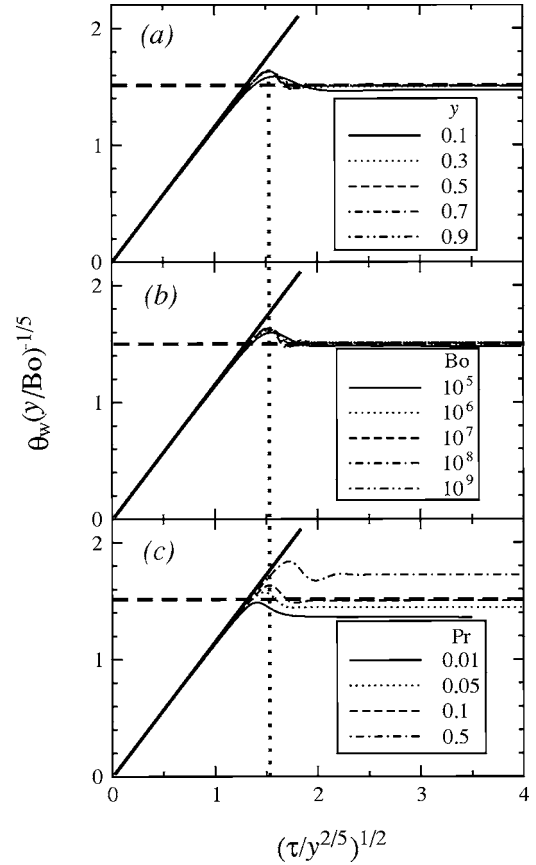

FIG. 5. DNS results for $\theta_w/(y/$Bo$)^{1/5}$ plotted against $(\tau/y^{2/5})^{1/2}$ with (a) the y variation at Bo$=10^7$ and Pr$=0.1$; (b) the Bo variation at $y=0.9$ and Pr$=0.1$; and (c) the Pr variation at Bo$/$Pr$=10^8$ and $y=0.9$. —— (bold), quantified scaling law $\theta_w=1.128\tau^{1/2}/Bo^{1/5}$; $\cdots\cdots$ (bold), quantified scaling law $\tau_{w,s}=2.339y^{2/5}$; – – – (bold), quantified scaling law $\theta_w=1.5105(y/$Bo$)^{1/5}$.

A. Verification and quantification of scaling laws

1. Scaling laws for θ_w, $\theta_{w,s}$, and $\tau_{w,s}$

The scaling laws obtained in the above scaling analysis for θ_w, the plate temperature scale at the start-up stage, and $\theta_{w,s}$, the plate temperature scale at the steady-state stage, are Eq. (20) and Eq. (26) respectively, and that for $\tau_{w,s}$, the time scale for the development of the plate temperature to reach the steady state, is Eq. (23).

Figure 5 presents the DNS results of the time series of θ_w with variations of y, Bo, and Pr in the ranges of $10^6 \leq$ Bo$/$Pr$\leq 10^{10}$ and $0.01 \leq$ Pr≤ 0.5, where θ_w and τ are scaled by $(y/$Bo$)^{1/5}$ and $y^{2/5}$, respectively. Figure 5(a) contains the DNS results of the time series of θ_w with the y variation at Bo$=10^7$ and Pr$=0.1$ (run 1), showing that at the start-up stage all five sets of data with different y fall onto the same straight line described by $\theta_w=1.128\tau^{1/2}/Bo^{1/5}$, which clearly demonstrates that θ_w has no dependence on y, meaning that the development of the wall temperature at this stage is one-dimensional, which is in agreement with the scaling law (20). At the steady-state stage, however, it is observed that the $y^{1/5}$ scaling brings all five sets of data with different y to fall onto approximately the same horizontal

line described by $\theta_{w,s}=1.5105(y/\mathrm{Bo})^{1/5}$, indicating that not only $\theta_{w,s}$ is y dependent and becomes two-dimensional but also the $y^{1/5}$ scaling is the correct y dependence of $\theta_{w,s}$, which agrees with the scaling law (26). When y decreases, it is observed that deviations from the scaling law will increase. (The DNS results show that the deviations of $\theta_{w,s}$ estimated by the scaling law (26) at $y=0.1$, 0.3, 0.5, and 0.7 are respectively, -2.70%, -0.68%, -0.45%, and -0.15% from that at $y=0.9$.) Furthermore, DNS results (not shown in the figure) also show that if $y\rightarrow0$ a significant deviation will be observed. The reason for this deviation is obvious, as when y approaches the leading edge ($y=0$) the boundary layer assumption made in the above scaling analysis will not hold anymore, as discussed in Sec. III C. The DNS results in the figure also show that the $y^{2/5}$ scaling is the correct y dependence of $\tau_{w,s}$, which confirms the scaling law (23).

Figure 5(b) contains the time series of θ_w with the Bo variation at $y=0.9$ and $\mathrm{Pr}=0.1$ (runs 1–5), showing that the $\mathrm{Bo}^{-1/5}$ scaling brings all five sets of data with different Bo to fall onto the same straight line described again by $\theta_w=1.128\tau^{1/2}/\mathrm{Bo}^{1/5}$ at the start-up stage and onto the same horizontal line described by $\theta_{w,s}=1.5105(y/\mathrm{Bo})^{1/5}$ at steady state respectively, indicating that the $\mathrm{Bo}^{-1/5}$ scaling is the correct Bo dependence of θ_w and $\theta_{w,s}$, which confirms the scaling laws (20) and (26). The DNS results in the figure also show that $\tau_{w,s}$ has no dependence on Bo, which is in agreement with the scaling law (23).

Figure 5(c) contains the time series of θ_w with the Pr variation at $y=0.9$ and $\mathrm{Bo}/\mathrm{Pr}=10^8$ (runs 6, 7, 3 and 8), clearly showing that $\theta_{w,s}$ has a further Pr dependence in addition to the $\mathrm{Pr}^{-1/5}$ scaling (the DNS results show that $\theta_{w,s}/(y/\mathrm{Bo})^{1/5}$ is 1.3725, 1.4537, 1.5105, and 1.7291 when Pr is 0.01, 0.05, 0.1, and 0.5, respectively), which is accounted for by the term $f_\theta(\mathrm{Pr})^{1/5}=[O(1)+O(\mathrm{Pr})]^{1/5}$ in the scaling law (26). It is also seen that $\tau_{w,s}$ is Pr dependent as the DNS results show that $\tau_{w,s}/y^{2/5}$ is 1.8930, 2.0940, 2.2425, and 2.8170 when Pr is 0.01, 0.05, 0.1, and 0.5, respectively, which is also accounted for by the term $f_{\tau,\theta}(\mathrm{Pr})^{2/5}=[O(1)+O(\mathrm{Pr})]^{2/5}$ in the scaling law (23).

The specific dependences of $f_\theta(\mathrm{Pr})$ and $f_{\tau,\theta}(\mathrm{Pr})$ on Pr can be determined with the DNS results, as shown in Fig. 6 where the DNS results of $f_\theta(\mathrm{Pr})$ and $f_{\tau,\theta}(\mathrm{Pr})$ are plotted against Pr for the Pr variation at $\mathrm{Bo}/\mathrm{Pr}=10^8$ and $y=0.9$, giving,

$$f_\theta(\mathrm{Pr})=5.2719+20.591\mathrm{Pr}, \tag{36}$$

$$f_{\tau,\theta}(\mathrm{Pr})=5.9671+17.917\mathrm{Pr}, \tag{37}$$

which indicate that the contribution from $O(\mathrm{Pr})$ in $f_\theta(\mathrm{Pr})$ or $f_{\tau,\theta}(\mathrm{Pr})$ is not negligible with respect to that from $O(1)$ and it increases with Pr. It is found that $f_\theta(\mathrm{Pr})$ and $f_{\tau,\theta}(\mathrm{Pr})$ estimated by Eqs. (36) and (37) are within $\pm2.38\%$ and $\pm4.71\%$, respectively, from their individual DNS results when Pr is in the range of 0.01 to 0.5. Hence, the scaling laws (23) and (26) are quantified as follows for $10^6\leqslant\mathrm{Bo}/\mathrm{Pr}\leqslant10^{10}$ and $0.01\leqslant\mathrm{Pr}\leqslant0.5$,
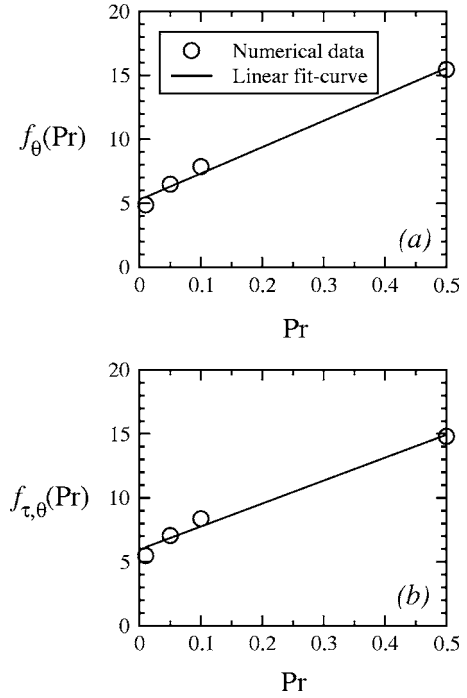
FIG. 6. DNS results for (a) $f_\theta(\mathrm{Pr})$ and (b) $f_{\tau,\theta}(\mathrm{Pr})$ plotted against Pr for the Pr variation at $\mathrm{Bo}/\mathrm{Pr}=10^8$ and $y=0.9$.

$$\theta_{w,s}=(5.2719+20.591\mathrm{Pr})^{1/5}\left(\frac{y}{\mathrm{Bo}}\right)^{1/5}, \tag{38}$$

$$\tau_{w,s}=(5.9671+17.917\mathrm{Pr})^{2/5}y^{2/5}. \tag{39}$$

It is therefore expected that the quantified scaling laws (38) and (39) will bring together all four sets of data with different Pr presented in Fig. 5(c). This is confirmed by the results shown in Fig. 7, where it is observed that all four sets of data with different Pr fall onto the same horizontal line described by Eq. (38) at steady state, all the time scales for different Pr have approximately the same value described by Eq. (39), and all four sets of data fall onto the same line described by the following equation at the start-up stage,
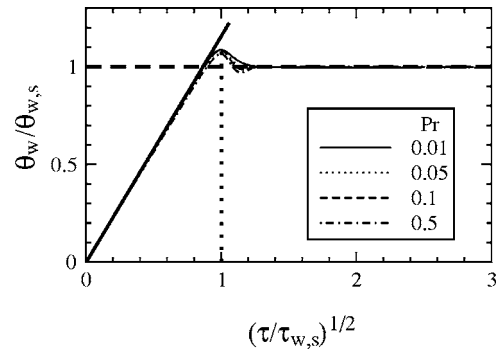

FIG. 7. DNS results for $\theta_w/\theta_{w,s}$ plotted against $(\tau/\tau_{m,s})^{1/2}$ with the Pr variation at $\mathrm{Bo}/\mathrm{Pr}=10^8$ and $y=0.9$. —— (bold), quantified scaling law $\theta_w=1.1492\tau^{1/2}/\mathrm{Bo}^{1/5}$; $\cdots\cdots$ (bold), quantified scaling law $\tau_{w,s}=f_{\tau,\theta}(\mathrm{Pr})^{2/5}y^{2/5}$; – – – (bold), quantified scaling law $\theta_{w,s}=f_\theta(\mathrm{Pr})^{1/5}(y/\mathrm{Bo})^{1/5}$.
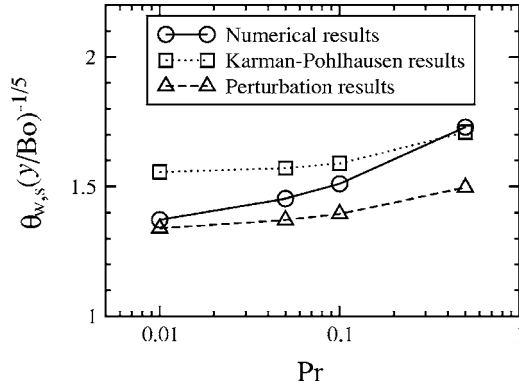
FIG. 8. DNS results and approximate solutions of $\theta_{w,s}(y/\text{Bo})^{-1/5}$ plotted against Pr for the Pr variation at $\text{Bo}/\text{Pr}=10^8$ and $y=0.9$.

$$\theta_w = 1.1617[f_\theta(\text{Pr})/f_{\tau,\theta}(\text{Pr})]^{1/5}\tau^{1/2}/\text{Bo}^{1/5}. \qquad (40)$$

Nevertheless, the DNS results show that $[f_\theta(\text{Pr})/f_{\tau,\theta}(\text{Pr})]^{1/5}$ varies from 0.97673 to 1.0087 with an average of 0.9892 (a change of within ±2%) when Pr changes from 0.01 to 0.5, indicating that this ratio is almost a constant in this Pr range and therefore at the start-up stage, θ_w can be approximated by

$$\theta_w = 1.1492\tau^{1/2}/\text{Bo}^{1/5}. \qquad (41)$$

As stated in Sec. III C, the similarity solution of Sparrow and Gregg [8], as shown by Eq. (32), includes such a further Pr dependence, that is,

$$\frac{\theta_{w,s}}{(y/\text{Bo})^{1/5}} = -5^{1/5}Pr^{2/5}F_\theta(\text{Pr}), \qquad (42)$$

although only the value of $F_\theta(\text{Pr})=-2.7507$ was obtained for Pr=0.1. Such further Pr dependencies were also predicted by the approximate solutions such as those obtained by the von Kármán-Pohlhausen method [8] and by the perturbation method [14] as shown by Eqs. (34) and (35), that is

$$\frac{\theta_{w,s}}{(y/\text{Bo})^{1/5}} = \frac{(360)^{1/5}}{2}(0.8+\text{Pr})^{1/5}, \qquad (43)$$

and

$$\frac{\theta_{w,s}}{(y/\text{Bo})^{1/5}} = 1.31411 + 0.257\text{Pr}^{1/2}. \qquad (44)$$

However, it is found that the predictions with these approximate solutions deviate considerably from the DNS results, as shown in Fig. 8 for the Pr variation at $\text{Bo}/\text{Pr}=10^8$ and $y=0.9$. It is further found that the approximate solution obtained by the von Kármán–Pohlhausen method becomes more accurate when Pr→1, while, on the other hand, that obtained by the perturbation method becomes more accurate when Pr→0, reflecting respectively their individual asymptotic behaviors.

2. Scaling laws for v_m, $v_{m,s}$, and $\tau_{m,s}$

The scaling laws obtained from the scaling analysis for v_m, the maximum vertical velocity scale at the startup stage,
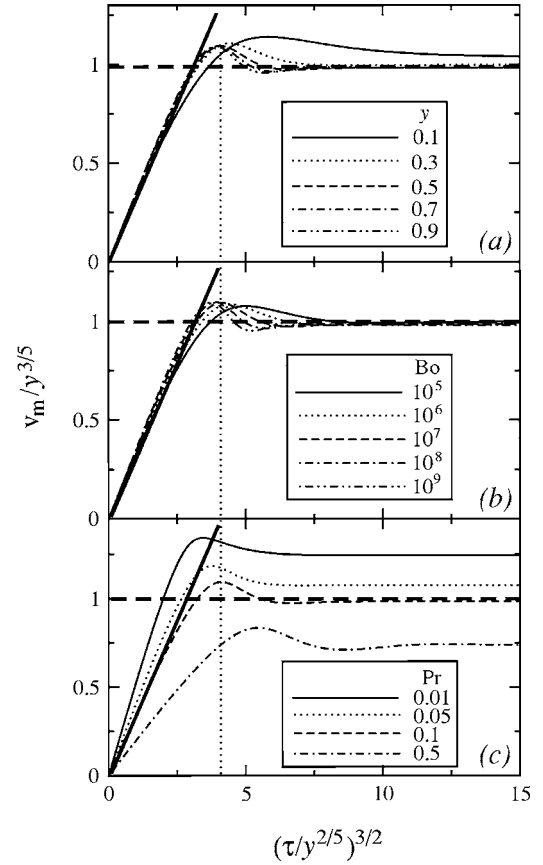

FIG. 9. DNS results for $v_m/y^{3/5}$ plotted against $(\tau/y^{2/5})^{3/2}$ with (a) the y variation at $\text{Bo}=10^7$ and $\text{Pr}=0.1$; (b) the Bo variation at $y=0.9$ and $\text{Pr}=0.1$; and (c) the Pr variation at $\text{Bo}/\text{Pr}=10^8$ and $y=0.9$. —— (bold), quantified scaling law $v_m=0.348\tau^{3/2}$; ····· (bold), quantified scaling law $\tau_{m,s}=2.477y^{2/5}$; – – – (bold), quantified scaling law $v_{m,s}=1.0172y^{3/5}$.

and $v_{m,s}$, the maximum vertical velocity scale at steady state, are Eq. (21) and Eq. (25), respectively, and that for $\tau_{m,s}$, the time scale for the development of the vertical velocity within the boundary layer to reach the steady state, is still Eq. (23).

Figure 9 presents the DNS results of the time series of v_m with variations of y, Bo, and Pr in the ranges of $10^6 \leqslant \text{Bo}/\text{Pr} \leqslant 10^{10}$ and $0.01 \leqslant \text{Pr} \leqslant 0.5$, where v_m and τ are scaled by $y^{3/5}$ and $y^{2/5}$, respectively. Figure 9(a) contains the time series of v_m with the y variation at $\text{Bo}=10^7$ and $\text{Pr}=0.1$, showing that at the start-up stage all five sets of data with different y fall onto the same straight line described by $v_m=0.348\tau^{3/2}$, which clearly demonstrates that v_m has no dependence on y and therefore is one-dimensional, agreeing with the scaling law (21). At steady state, it is observed that the $y^{3/5}$ scaling brings all five sets of data with different y to fall onto approximately the same horizontal line described by $v_{m,s}=1.0172y^{3/5}$, indicating that not only $v_{m,s}$ is y dependent and therefore two-dimensional but also the $y^{3/5}$ scaling is the correct y dependence of $v_{m,s}$, which agrees with the scaling law (25), although deviations from the scaling law are observed at small y [the DNS results show that the deviations of $v_{m,s}$ estimated by the scaling law (25) at $y=0.1, 0.3, 0.5,$ and 0.7 are 5.60%, 1.52%, 0.02%, and −0.01%, respectively, from that at $y=0.9$], due to the same reason as discussed
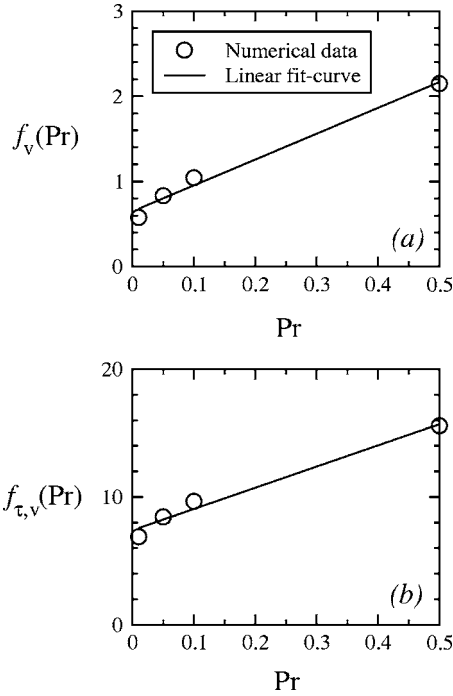
FIG. 10. DNS results for (a) $f_v(\text{Pr})$ and (b) $f_{\tau,v}(\text{Pr})$ plotted against Pr for the Pr variation at $\text{Bo}/\text{Pr}=10^8$ and $y=0.9$.

above for the $\theta_{w,s}$ case. The DNS results also show that the $y^{2/5}$ scaling is the correct y dependence of $\tau_{m,s}$, which confirms the scaling law (23), although, similar to $v_{m,s}$, deviations from the scaling law (23) are also observed at small y.

Figure 9(b) contains the time series of v_m with the Bo variation at $y=0.9$ and $\text{Pr}=0.1$, showing that both v_m and $v_{m,s}$ have no Bo dependence for a fixed Pr as all five sets of data with different Bo when $\text{Pr}=0.1$ fall onto the same straight line described by $v_m=0.348\tau^{3/2}$ at the start-up stage and onto the same horizontal line described by $v_{m,s}=1.0172y^{3/5}$ at steady state respectively, which agrees with the scaling laws (21) and (25). The DNS results in the figure also show that $\tau_{m,s}$ has no dependence on Bo when Pr is fixed, which is in agreement with the scaling law (23), although deviation between the DNS results and the scaling law (23) can be observed when Bo decreases while Pr is fixed.

Figure 9(c) contains the time series of v_m with the Pr variation at $y=0.9$ and $\text{Bo}/\text{Pr}=10^8$, clearly showing that v_m, $v_{m,s}$, and $\tau_{m,s}$ are Pr dependent, as predicted by the terms $f_v'(\text{Pr})=O(1)+O(\text{Pr})$, $f_v(\text{Pr})^{2/5}=[O(1)+O(\text{Pr})]^{2/5}$, and $f_{\tau,v}(\text{Pr})^{2/5}=[O(1)+O(\text{Pr})]^{2/5}$, respectively, presented in the scaling laws (21), (23), and (25).

The specific dependences of $f_v(\text{Pr})$ and $f_{\tau,v}(\text{Pr})$ on Pr can be determined with the DNS results, as shown in Fig. 10 where the DNS results of $f_v(\text{Pr})$ and $f_{\tau,v}(\text{Pr})$ are plotted against Pr for the Pr variation at $\text{Bo}/\text{Pr}=10^8$ and $y=0.9$, giving,

$$f_v(\text{Pr}) = 0.6491 + 3.0336\text{Pr}, \tag{45}$$

$$f_{\tau,v}(\text{Pr}) = 7.402 + 16.594\text{Pr}, \tag{46}$$

which, similar to the above θ_w case, also show that the contribution from $O(\text{Pr})$ in $f_v(\text{Pr})$ or $f_{\tau,v}(\text{Pr})$ is not negligible
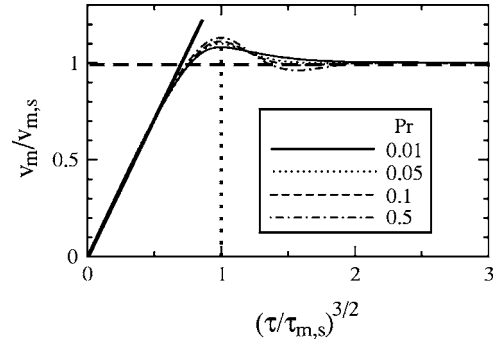

FIG. 11. DNS results for $v_m/v_{m,s}$ plotted against $(\tau/\tau_{m,s})^{3/2}$ for the Pr variation at $\text{Bo}/\text{Pr}=10^8$ and $y=0.9$. —— (bold), quantified scaling law $v_m=1.4232\tau^{3/2}/f_v'(\text{Pr})$; $\cdots\cdots$ (bold), quantified scaling law $\tau_{m,s}=f_{\tau,v}(\text{Pr})^{2/5}y^{2/5}$; $---$ (bold), quantified scaling law $v_{m,s}=y^{3/5}/f_v(\text{Pr})^{2/5}$.

with respect to that from $O(1)$ and it increases with Pr. It is found that $f_v(\text{Pr})$ and $f_{\tau,v}(\text{Pr})$ estimated by Eqs. (45) and (46) are within $\pm6.32\%$ and $\pm3.82\%$, respectively, from their individual DNS results when Pr is in the range of 0.01 to 0.5. Hence, the scaling laws (23) and (25) are quantified as follows for $10^6 \leqslant \text{Bo}/\text{Pr} \leqslant 10^{10}$ and $0.01 \leqslant \text{Pr} \leqslant 0.5$,

$$v_{m,s} = \frac{y^{3/5}}{(0.6491 + 3.0336\text{Pr})^{2/5}}, \tag{47}$$

$$\tau_{m,s} = (7.402 + 16.594\text{Pr})^{2/5}y^{2/5}. \tag{48}$$

It is therefore expected that the quantified scaling laws (47) and (48) will bring together all four sets of data with different Pr presented in Fig. 9(c). This is confirmed by the results shown in Fig. 11, where it is observed that all four sets of data with different Pr fall onto the same horizontal line described by Eq. (47) at steady state, all the time scales for different Pr have approximately the same value described by Eq. (48), and all four sets of data fall onto the same line described by the following equation at the start-up stage,

$$v_m = 1.4232\frac{\tau^{3/2}}{f_v(\text{Pr})^{2/5}f_{\tau,v}(\text{Pr})^{3/5}}. \tag{49}$$

Nevertheless, the DNS results show that $f_v'(\text{Pr})$ $=f_v(\text{Pr})^{2/5}f_{\tau,v}(\text{Pr})^{3/5}$ can be approximated by the following equation for Pr in the range of $0.01 \leqslant \text{Pr} \leqslant 0.5$,

$$f_v'(\text{Pr}) = 2.8071 + 8.6105\text{Pr}, \tag{50}$$

which is in agreement with the scaling law (21).

The dependence of $v_{m,s}$ on Pr was also predicted by the similarity solution obtained by Sparrow and Gregg [8] who showed that at steady state the horizontal profile of the vertical velocity within the boundary layer is described by

$$v(x,y) = 5^{3/5}\text{Pr}^{1/5}F(x,\text{Pr})y^{3/5}, \tag{51}$$

where $F(x,\text{Pr})$ is a function of x and Pr which can be obtained by simultaneously solving two ordinary differential equations [the Eqs. (3a) and (3b) subject to the boundary conditions (11) in Ref. [8]].
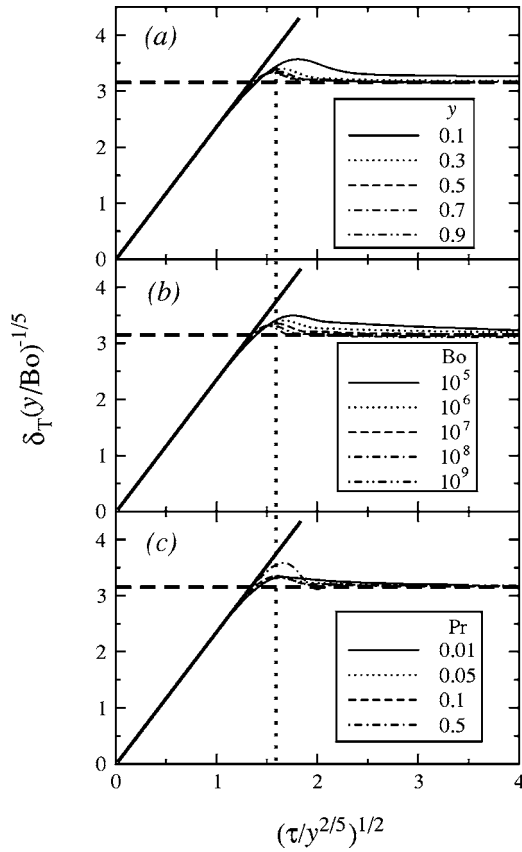
FIG. 12. DNS results for $\delta_T(y/\text{Bo})^{-1/5}$ plotted against $(\tau/y^{2/5})^{1/2}$ with (a) the y variation at $\text{Bo}=10^7$ and $\text{Pr}=0.1$; (b) the Bo variation at $y=0.9$ and $\text{Pr}=0.1$; and (c) the Pr variation at $\text{Bo}/\text{Pr}=10^8$ and $y=0.9$. —— (bold), quantified scaling law $\delta_T=2.339\tau^{1/2}/\text{Bo}^{1/5}$; ··· ··· (bold), quantified scaling law $\tau_{T,s}=2.5823y^{2/5}$; – – – (bold), quantified scaling law $\delta_{T,s}=3.1572(y/\text{Bo})^{1/5}$.

3. Scaling laws for δ_T, $\delta_{T,s}$, and $\tau_{T,s}$

The scaling laws obtained in the above scaling analysis for δ_T, the thermal boundary-layer thickness scale at the start-up stage, and $\delta_{T,s}$, the thermal boundary-layer thickness scale at steady state, are Eq. (19) and Eq. (24), respectively, and that for $\tau_{T,s}$, the time scale for the development of the thermal boundary-layer to reach the steady state, is again Eq. (23).

Figure 12 presents the DNS results of the time series of δ_T with variations of y, Bo, and Pr in the ranges of $10^6 \leqslant \text{Bo}/\text{Pr} \leqslant 10^{10}$ and $0.01 \leqslant \text{Pr} \leqslant 0.5$, where δ_T and τ are scaled by $(y/\text{Bo})^{1/5}$ and $y^{2/5}$, respectively. Figure 12(a) contains the time series of δ_T with the y variation at $\text{Bo}=10^7$ and $\text{Pr}=0.1$, showing that at the start-up stage all five sets of data with different y fall onto the same straight line described by $\delta_T=2.339\tau^{1/2}/\text{Bo}^{1/5}$, which clearly demonstrates that δ_T has no dependence on y and is one-dimensional, agreeing with the scaling law (19). At steady state, it is found that the $y^{1/5}$ scaling brings all five sets of data with different y to fall onto approximately the same horizontal line described by $\delta_{T,s}=3.1516(y/\text{Bo})^{1/5}$, indicating that not only $\delta_{T,s}$ is y dependent and two-dimensional but also the $y^{1/5}$ scaling is the correct y dependence of $\delta_{T,s}$, which agrees with the scaling

law (24). When y decreases, it is observed that deviation from the scaling law increases [the DNS results show that the deviations of $\delta_{T,s}$ estimated by the scaling law (24) at $y=0.1$, 0.3, 0.5, and 0.7 are respectively, 6.50%, 3.21%, 1.87%, and 1.11% from that at $y=0.9$]. The reason for this increasing deviation with decreasing y is the same as for the θ_w case as discussed above.

Figure 12(b) contains the time series of δ_T with the Bo variation at $y=0.9$ and $\text{Pr}=0.1$, showing that the $\text{Bo}^{-1/5}$ scaling brings all five sets of data with different Bo/Pr to fall onto the same straight line described again by $\delta_T=2.339\tau^{1/2}/\text{Bo}^{1/5}$ at the start-up stage and onto the same horizontal line described by $\delta_{T,s}=3.1516(y/(\text{Bo})^{1/5}$ at steady state respectively, indicating that the $\text{Bo}^{-1/5}$ scaling is the correct Bo dependence of δ_T and $\delta_{T,s}$, which confirms the scaling laws (19) and (24), although for $\text{Bo}=10^5$ a relatively large deviation is observed (the DNS results show that the deviations of $\delta_{T,s}$ estimated by the scaling law (24) at $\text{Bo}=10^5$, 10^6, 10^7, and 10^8 are 3.77%, 0.56%, 0.71% and 0.55%, respectively, from that at $\text{Bo}=10^9$). Further DNS results (not shown in the figure) show that for Bo smaller than 10^5 such a deviation will become significant. This is due to the fact that when Bo decreases, as stated in Sec. III C, the deviation from the boundary layer assumption made in the scaling analysis, which requires that $\text{Bo} \gg 1$ to ensure $\delta_T \ll 1$, will increase rapidly.

Similar observations can also be obtained from Fig. 12(c) with the Pr variation where the DNS results at $y=0.9$ and $\text{Bo}/\text{Pr}=10^8$ are presented for $\text{Pr}=0.01$, 0.05, 0.1, and 0.5. However, the DNS results show that $f_T(\text{Pr})=O(1)+O(\text{Pr})$ in the scaling law (24) is approximately constant for the four Pr values $[f_T(\text{Pr})^{1/5}=3.1486$, 3.1476, 3.1516, and 3.1810 for $\text{Pr}=0.01$, 0.05, 0.1, and 0.5, respectively, with an average of 3.1572]. Hence, the contribution from $O(\text{Pr})$ in $f_T(\text{Pr})$ is negligible with respect to that from $O(1)$, unlike the θ_w and v_m cases as discussed above. Similarly, it is also found that $f_{\tau,T}(\text{Pr})=O(1)+O(\text{Pr})$ in the scaling law (23) is approximately constant for the four Pr values $[f_{\tau,T}(\text{Pr})^{2/5}=2.7599$, 2.4751, 2.3969, and 2.6973 for $\text{Pr}=0.01$, 0.05, 0.1, and 0.5, respectively, with an average of 2.5823]. Hence, the scaling laws (23) and (24) are respectively quantified by

$$\delta_{T,s} = 3.1572\left(\frac{y}{\text{Bo}}\right)^{1/5}, \qquad (52)$$

$$\tau_{T,s} = 2.5823y^{2/5}, \qquad (53)$$

for $10^6 \leqslant \text{Bo}/\text{Pr} \leqslant 10^{10}$ and $0.01 \leqslant \text{Pr} \leqslant 0.5$.

4. Scaling laws for δ_{vi}, $\delta_{vi,s}$, and $\tau_{vi,s}$

As shown in the above scaling analysis, the scaling laws for δ_{vi}, $\delta_{vi,s}$, and $\tau_{vi,s}$, which are respectively the inner velocity boundary-layer thickness scales at the start-up stage and at steady state, and the time scale for the inner velocity boundary-layer development to reach the steady state, are Eqs. (22), (23), and (27).

Figure 13 presents the DNS results of the time series of δ_{vi} with variations of y, Bo, and Pr in the ranges of $10^6 \leqslant \text{Bo}/\text{Pr} \leqslant 10^{10}$ and $0.01 \leqslant \text{Pr} \leqslant 0.5$, where δ_{vi} and τ are
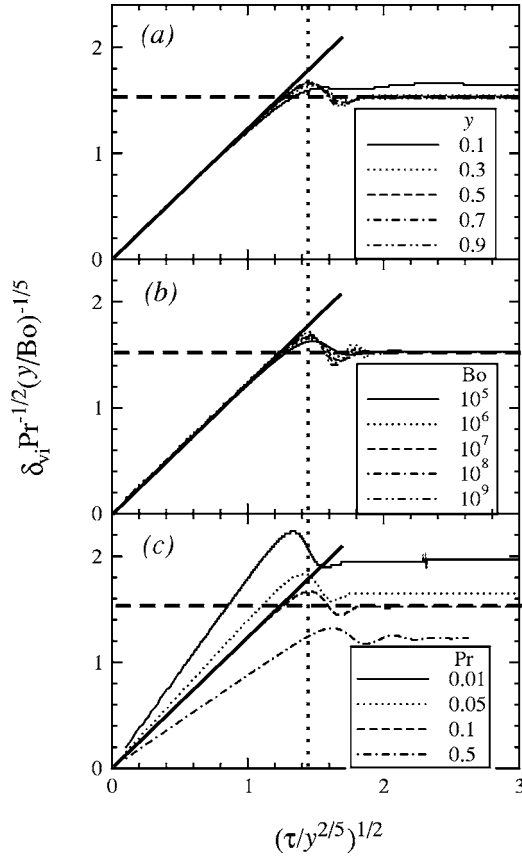
FIG. 13. DNS results for $\delta_{vi}/[Pr^{1/2}(y/Bo)^{1/5}]$ plotted against $(\tau/y^{2/5})^{1/2}$ with (a) the y variation at Bo$=10^7$ and Pr$=0.1$; (b) the Bo variation at $y=0.9$ and Pr$=0.1$; and (c) the Pr variation at Bo/Pr$=10^8$ and $y=0.9$. —— (bold), quantified scaling law δ_{vi} $=0.835Pr^{1/2}\tau^{1/2}/Bo^{1/5}$; $\cdots\cdots$ (bold), quantified scaling law $\tau_{vi,s}$ $=2.152y^{2/5}$; $–\,–\,–$ (bold), quantified scaling law $\delta_{vi,s}$ $=1.549Pr^{1/2}(y/Bo)^{1/5}$.

FIG. 14. DNS results for (a) $C(Pr)$ plotted against $Pr^{-1/8}$ and (b) $f_{\tau,vi}(Pr)$ plotted against Pr for the Pr variation at Bo/Pr$=10^8$ and $y=0.9$.

scaled by $Pr^{1/2}(y/Bo)^{1/5}$ and $y^{2/5}$, respectively. Figure 13(a) contains the time series of δ_{vi} with the y variation at Bo $=10^7$ and Pr$=0.1$, showing that at the start-up stage all five sets of data with different y fall onto the same straight line described by $\delta_{vi}=0.835\tau^{1/2}Pr^{1/2}/Bo^{1/5}$, which clearly confirms that the scaling law (22) is y independent. However, the scaling analysis shows that at steady state the scaling law (27) becomes y dependent, which is confirmed by the DNS results, as shown in the figure, as all five sets of data with different y fall approximately onto the same horizontal line described by $\delta_{vi,s}=1.549Pr^{1/2}(y/Bo)^{1/5}$, although large deviations from the scaling law are observed at small y [the DNS results show that the deviations of $\delta_{vi,s}$ estimated by the scaling law (27) at $y=0.1$, 0.3, 0.5, and 0.7 are 11.73%, 3.62%, 2.69%, and 0.51%, respectively, from that at $y=0.9$] for the same reason as discussed above. The DNS results in the figure also show that the $y^{2/5}$ scaling is the correct y dependence of $\tau_{vi,s}$, which confirms the scaling law (23).

Figure 13(b) contains the time series of δ_{vi} with the Bo variation at $y=0.9$ and Pr$=0.1$, showing that the Bo$^{-1/5}$ scaling brings all five sets of data with different Bo to fall onto the same straight line described again by δ_{vi} $=0.835\tau^{1/2}Pr^{1/2}/Bo^{1/5}$ at the start-up stage and onto the same
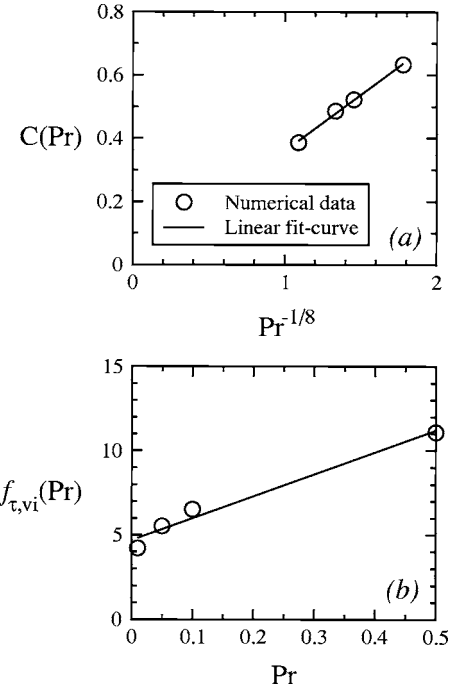
horizontal line described by $\delta_{vi,s}=1.549Pr^{1/2}(y/Bo)^{1/5}$ respectively, indicating that the Bo$^{-1/5}$ scaling is the correct Bo dependence of δ_{vi} and $\delta_{vi,s}$, which confirms the scaling laws (22) and (27). The DNS results in the figure also show that $\tau_{vi,s}$ has no dependence on Bo, which is in agreement with the scaling law (23).

Figure 13(c) contains the time series of δ_{vi} with the Pr variation at $y=0.9$ and Bo/Pr$=10^8$, clearly showing that $\delta_{vi,s}$ has a further Pr dependence in addition to the $Pr^{1/2}/Bo^{1/5}$ scaling, which is accounted for by the term $[O(1)+O(Pr)]^{1/5}$, and $\tau_{vi,s}$ is also Pr dependent, which is accounted for by the term $[O(1)+O(Pr)]^{2/5}$, agreeing with the scaling laws (23) and (27).

The scaling analysis indicates that $\delta_{vi,s}=CPr^{1/2}\delta_{T,s}$, as shown by the scaling law (27), where C is a constant of proportionality. However, the DNS results show that C $=0.6328$, 0.5225, 0.4863, and 0.3863 for Pr$=0.01$, 0.05, 0.1, and 0.5, respectively, which clearly shows that C is not a constant but monotonically decreases with Pr. In the scaling analysis, the scaling law (27) was obtained assuming a dominant inertia-friction balance in the inner velocity boundary layer. It has then been assumed that the thickness of the inner velocity boundary layer is characterized by the distance from the boundary to the position where the vertical velocity is maximum. The results shown here clearly demonstrate that this is not the appropriate length scale, and it is at present unclear how such a length scale should be obtained from the DNS. Nevertheless, for completeness, we will develop an empirical scaling for this velocity length scale, as follows.

The DNS results, as shown in Fig. 14(a), give the following empirical expression for $C(Pr)$,
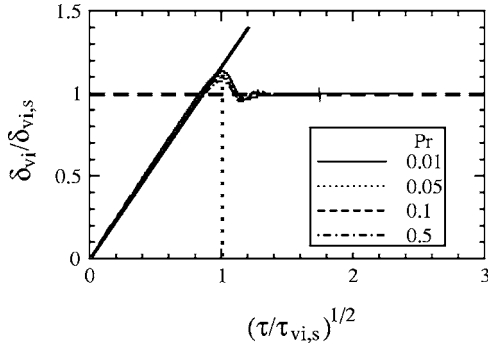
FIG. 15. DNS results for $\delta_{vi}/\delta_{vi,s}$ plotted against $(\tau/\tau_{vi,s})^{1/2}$ with the Pr variation at Bo/Pr$=10^8$ and $y=0.9$. —— (bold), quantified scaling law $\delta_{vi}=0.9185\text{Pr}^{3/8}\tau^{1/2}f_{\tau,vi}(\text{Pr})^{-2/5}\text{Bo}^{-1/5}$; $\cdots\cdots$ (bold), quantified scaling law $\tau_{w,s}=f_{\tau,vi}(\text{Pr})^{2/5}y^{2/5}$; $---$ (bold), quantified scaling law $\delta_{vi,s}=1.1233\text{Pr}^{3/8}(y/\text{Bo})^{1/5}$.

$$C(\text{Pr}) = 0.3558\text{Pr}^{-1/8}, \qquad (54)$$

which is found to be within $\pm2.42\%$ from the DNS results for Pr in the range of 0.01 to 0.5. However, the DNS results show that $f_{\tau,vi}(\text{Pr})=O(1)+O(\text{Pr})$ in the scaling law (23) for $\tau_{vi,s}$ has the following quantified form, as shown in Fig. 14(b),

$$f_{\tau,v}(\text{Pr}) = 7.402 + 16.594\text{Pr}, \qquad (55)$$

which, similar to the above θ_w and v_m cases, also show that the contribution from $O(\text{Pr})$ in $f_{\tau,vi}(\text{Pr})$ is not negligible with respect to that from $O(1)$ and it increases with Pr. It is found that $f_{\tau,v}(\text{Pr})$ estimated by Eq. (55) is within $\pm5.50\%$ from the DNS results when Pr is in the range of 0.01 to 0.5. Hence, the scaling law (27) has the following quantified expression for $10^6\leqslant\text{Bo}/\text{Pr}\leqslant10^{10}$ and $0.01\leqslant\text{Pr}\leqslant0.5$

$$\delta_{vi,s} = C(\text{Pr})\text{Pr}^{1/2}\delta_{T,s} = 1.1233\text{Pr}^{3/8}\left(\frac{y}{\text{Bo}}\right)^{1/5}, \qquad (56)$$

and the scaling law (23) for $\tau_{vi,s}$ has the following form,

$$\tau_{vi,s} = (4.691 + 13.023\text{Pr})^{2/5}y^{2/5}. \qquad (57)$$

It is therefore expected that the modified scaling laws (56) and (57) will bring together all four sets of data with different Pr presented in Fig. 13(c). This is confirmed by the results shown in Fig. 15, where it is observed that all four sets of scaled data with different Pr to fall onto the same horizontal line described by Eq. (56) at steady state and the same straight line described by

$$\delta_{vi} = 0.9185\frac{\text{Pr}^{3/8}\tau^{1/2}}{f_{\tau,vi}(\text{Pr})^{2/5}\text{Bo}^{1/5}}, \qquad (58)$$

at the start-up stage.

5. Scaling laws for δ_{vo}

At steady state for Pr<1 it is expected that the outer velocity boundary layer thickness, $\delta_{vo,s}$, will match the thermal boundary layer thickness, $\delta_{T,s}$. During development it is
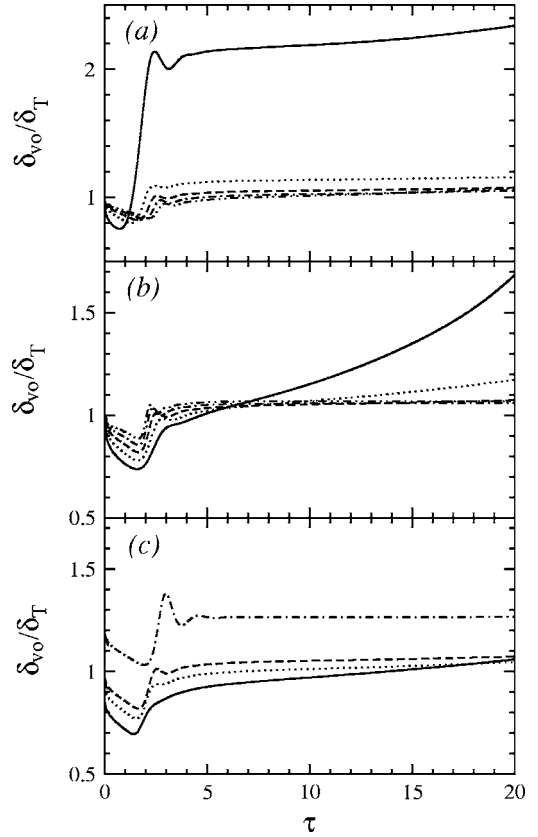

FIG. 16. DNS results for δ_{vo}/δ_T with (a) the y variation at Bo $=10^7$ and Pr$=0.1$ (——, $y=0.1$; $\cdots\cdots$, $y=0.3$; ——, $y=0.5$; $-\cdot-$, $y=0.7$; $-\cdot\cdot-$, $y=0.9$); (b) the Bo variation at $y=0.5$ and Pr$=0.1$ (——, Bo$=10^5$; $\cdots\cdots$, Bo$=10^6$; ——, Bo$=10^7$; $-\cdot-$, Bo$=10^8$; $-\cdot\cdot-$, Bo$=10^9$); and (c) the Pr variation at $y=0.5$ and Bo/Pr$=10^8$ (——, Pr$=0.01$; $\cdots\cdots$, Pr$=0.05$; ——, Pr$=0.1$; $-\cdot-$, Pr$=0.5$).

expected that the outer velocity boundary layer thickness δ_{vo} will lie between that of the inner velocity boundary layer, δ_{vi}, and the thermal boundary layer thickness δ_T. The outer velocity boundary layer thickness at steady state is therefore expected to obey the same scaling laws as the steady-state thermal boundary layer thickness. Time series for δ_{vo}/δ_T are shown in Fig. 16 for the variations of y, Bo, and Pr in the ranges of $10^6\leqslant\text{Bo}/\text{Pr}\leqslant10^{10}$ and $0.01\leqslant\text{Pr}\leqslant0.5$. It is seen that at full development the small y and small Bo/Pr results show that δ_{vo}/δ_T is considerably greater than 1.0, indicating that the scaling is not correct for these values, which as noted above is expected as the scaling will not hold in the nonsimilar region of the flow. The Pr variation results are presented for $y=0.5$ and Bo/Pr$=10^8$, values for which similarity is expected to hold. In this case the scaling predicts that $\delta_{vo}/\delta_T\simeq1.0$ is independent of Pr. This is seen to be true for all except the largest Prandtl number, Pr$=0.5$. The scaling is expected to break done in the region of Pr$=1.0$, as it is known that for Pr>1.0, the ratio δ_{vo}/δ_T is Pr dependent. The unsteady variation of δ_{vo}/δ_T prior to full development shows a complex structure with δ_{vo}/δ_T dependent on Pr, however it is seen that for all except Pr$=0.5$ $\delta_{vo}/\delta_T\leqslant1.0$ during the flow development stage.
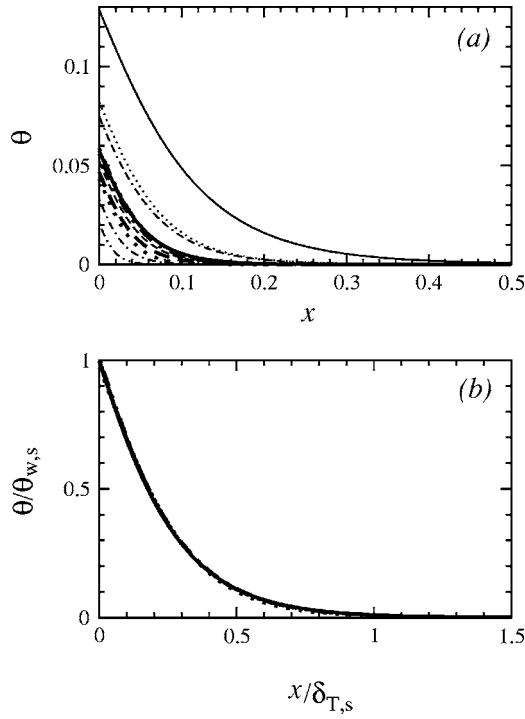
FIG. 17. DNS results of horizontal temperature profiles within the thermal boundary layer at steady state for selected values of Bo, Pr, and y: (a) θ plotted against x; (b) $\theta/\theta_{w,s}$ plotted against $x/\delta_{T,s}$. ——, Bo$=10^5$, Pr$=0.1$ and $y=0.5$; $\cdots\cdots$, Bo$=10^6$, Pr$=0.1$ and $y=0.5$; ——, Bo$=10^7$, Pr$=0.1$ and $y=0.5$; --, Bo$=10^8$, Pr$=0.1$ and $y=0.5$; --·--, Bo$=10^9$, Pr$=0.1$ and $y=0.5$; ——, Bo$=10^6$, Pr$=0.01$ and $y=0.5$; —— (bold), Bo$=5\times10^6$, Pr$=0.05$ and $y=0.5$; $\cdots\cdots$ (bold), Bo$=5\times10^7$, Pr$=0.5$ and $y=0.5$; —— (bold), Bo$=10^7$, Pr$=0.1$ and $y=0.3$; --· (bold), Bo$=10^7$, Pr$=0.1$ and $y=0.7$; --·-- (bold), Bo$=10^7$, Pr$=0.1$ and $y=0.9$.

B. Similarity of temperature and vertical velocity profiles

1. Similarity of temperature profiles

Figure 17 contains the numerically simulated horizontal temperature profiles within the thermal boundary layer at the steady state for the selected values of Bo, Pr, and y. The numerical results presented in Fig. 17(b), where θ and x are scaled by $\theta_{w,s}$ and $\delta_{T,s}$ respectively, show that the scales $\theta_{w,s}$ and $\delta_{T,s}$ collapse all sets of data onto a single curve, indicating that the temperature similarity is well preserved within the thermal boundary layer at the steady state, that is, the horizontal temperature profile within the thermal boundary layer at the steady state can be expressed as follows

$$\frac{\theta}{\theta_{w,s}} = f\left(\frac{x}{\delta_{T,s}}\right), \tag{59}$$

where $f(x/\delta_{T,s})$ represents some function of $x/\delta_{T,s}$.

Figure 18 contains the numerically simulated horizontal temperature profiles within the thermal boundary layer at the start-up stage for the selected values of Bo, Pr, y, and τ. The numerical results presented in Fig. 18(b), where θ and x are scaled by θ_w and δ_T, respectively, show that the scales θ_w and δ_T collapse all sets of data onto a single curve, indicating that the temperature similarity is also well preserved within the
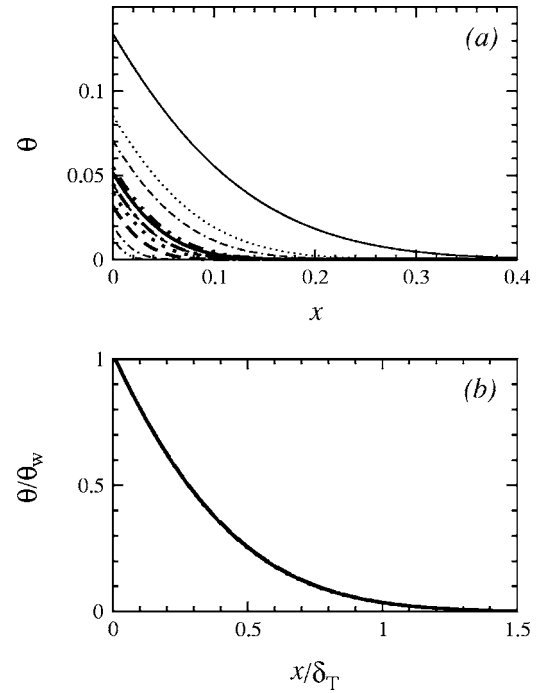

FIG. 18. DNS results of horizontal temperature profiles within the thermal boundary layer at the start-up stage for selected values of Bo, Pr, y and τ: (a) θ plotted against x; (b) θ/θ_w plotted against x/δ_T. ——, Bo$=10^5$, Pr$=0.1$ and $y=0.5$ at $\tau=1.5$; $\cdots\cdots$, Bo$=10^6$, Pr$=0.1$ and $y=0.5$ at $\tau=1.5$; ——, Bo$=10^7$, Pr$=0.1$ and $y=0.5$ at $\tau=1.0$; --, Bo$=10^8$, Pr$=0.1$ and $y=0.5$ at $\tau=0.5$; --·--, Bo$=10^9$, Pr$=0.1$ and $y=0.5$ at $\tau=0.5$; ——, Bo$=10^6$, Pr$=0.01$ and $y=0.5$ at $\tau=1.0$; —— (bold), Bo$=5\times10^6$, Pr$=0.05$ and $y=0.5$ at $\tau=1.0$; $\cdots\cdots$ (bold), Bo$=5\times10^7$, Pr$=0.5$ and $y=0.5$ at $\tau=1.5$; —— (bold), Bo$=10^7$, Pr$=0.1$ and $y=0.3$ at $\tau=0.5$; --· (bold), Bo$=10^7$, Pr$=0.1$ and $y=0.7$ at $\tau=1.0$; --·-- (bold), Bo$=10^7$, Pr$=0.1$ and $y=0.9$ at $\tau=1.5$.

thermal boundary layer at the start-up stage, that is, the horizontal temperature profile within the thermal boundary layer at the start-up stage can be expressed as follows

$$\frac{\theta}{\theta_w} = f\left(\frac{x}{\delta_T}\right), \tag{60}$$

where $f(x/\delta_T)$ represents some function of x/δ_T.

2. Similarity of vertical velocity profiles

Figure 19 contains the numerically simulated horizontal vertical velocity profiles within the viscous boundary layer at the steady state for the selected values of Bo, Pr, and y. The numerical results presented in Fig. 19(a), where the horizontal vertical velocity profiles within the inner viscous boundary layer at the steady state are presented, and v and x are scaled by $v_{m,s}$ and $\delta_{vi,s}$, respectively, show that the scales $v_{m,s}$ and $\delta_{vi,s}$ collapse all sets of data onto a single curve, indicating that the vertical velocity similarity is well preserved within the inner viscous boundary layer at the steady state, that is, the horizontal vertical velocity profile within the inner viscous boundary layer at the steady state can be expressed as follows
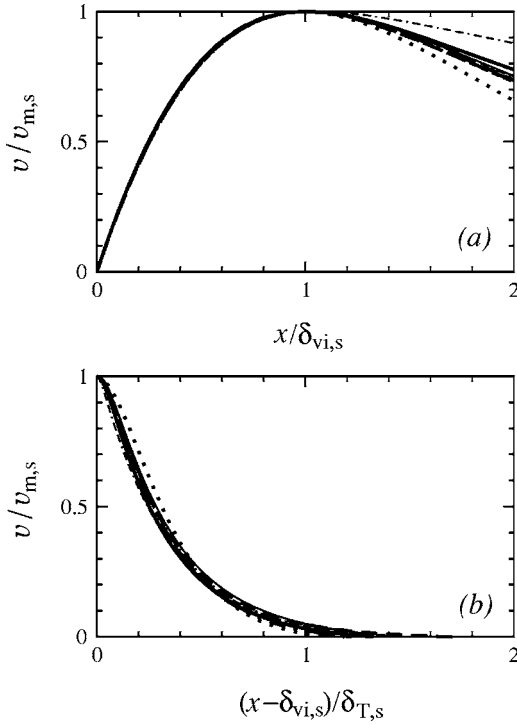
FIG. 19. DNS results of horizontal profiles of the vertical velocity within the velocity boundary layer at steady state for selected values of Bo, Pr and y: (a) $v/v_{m,s}$ plotted against $x/\delta_{vi,s}$ within the inner velocity boundary layer; (b) $v/v_{m,s}$ plotted against $(x-\delta_{vi,s})/\delta_{T,s}$ within the outer velocity boundary layer. ——, Bo $=10^5$, Pr$=0.1$ and $y=0.5$; $\cdots\cdots$, Bo$=10^6$, Pr$=0.1$ and $y=0.5$; ——, Bo$=10^7$, Pr$=0.1$ and $y=0.5$; –·–, Bo$=10^8$, Pr$=0.1$ and $y=0.5$; –··–, Bo$=10^9$, Pr$=0.1$ and $y=0.5$; ——·—, Bo$=10^6$, Pr$=0.01$ and $y=0.5$; —— (bold), Bo$=5\times10^6$, Pr$=0.05$ and $y=0.5$; $\cdots\cdots$ (bold), Bo $=5\times10^7$, Pr$=0.5$ and $y=0.5$; —— (bold), Bo$=10^7$, Pr$=0.1$ and $y=0.3$; –·– (bold), Bo$=10^7$, Pr$=0.1$ and $y=0.7$; –··– (bold), Bo$=10^7$, Pr$=0.1$ and $y=0.9$.

$$\frac{v}{v_{m,s}} = f\left(\frac{x}{\delta_{vi,s}}\right), \qquad (61)$$

where $f(x/\delta_{vi,s})$ represents some function of $x/\delta_{vi,s}$. Figure 19(b), where the horizontal vertical velocity profiles within the outer viscous boundary layer at the steady state are presented, and v and $(x-\delta_{vi,s})$ are scaled by $v_{m,s}$ and $\delta_{T,s}$ respectively, show that the scales $v_{m,s}$ and $\delta_{T,s}$ satisfactorily collapse all sets of data onto a single curve, indicating that the vertical velocity similarity is also well preserved within the outer viscous boundary layer at the steady state, that is, the horizontal vertical velocity profile within the outer viscous boundary layer at the steady state can be expressed as follows

$$\frac{v}{v_{m,s}} = f\left(\frac{x-\delta_{vi,s}}{\delta_{T,s}}\right), \qquad (62)$$

where $f\left[(x-\delta_{vi,s})/\delta_{T,s}\right]$ represents some function of $(x-\delta_{vi,s})/\delta_{T,s}$.

Figure 20 contains the numerically simulated horizontal vertical velocity profiles within the viscous boundary layer at
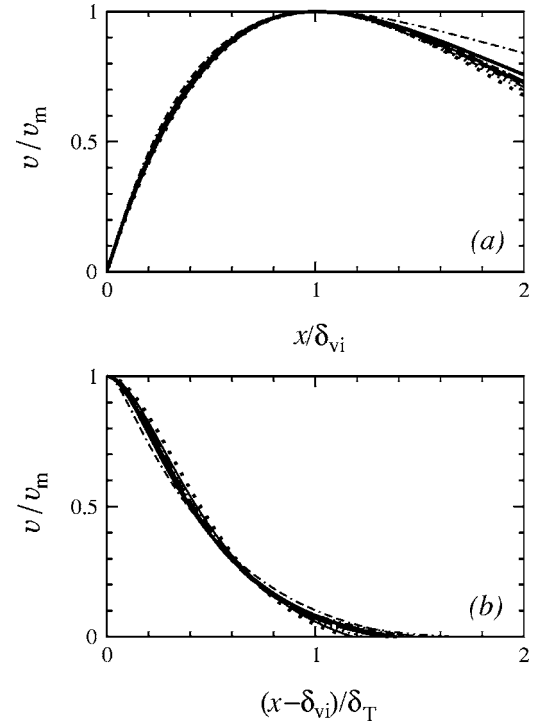
FIG. 20. DNS results of horizontal profiles of the vertical velocity within the velocity boundary layer at the start-up stage for selected values of Bo, Pr, y and τ: (a) v/v_m plotted against x/δ_{vi} within the inner velocity boundary layer; (b) v/v_m plotted against $(x-\delta_{vi})/\delta_T$ within the outer velocity boundary layer. ——, Bo $=10^5$, Pr$=0.1$ and $y=0.5$ at $\tau=1.5$; $\cdots\cdots$, Bo$=10^6$, Pr$=0.1$ and $y=0.5$ at $\tau=1.5$; ——, Bo$=10^7$, Pr$=0.1$ and $y=0.5$ at $\tau=1.0$; –·–, Bo$=10^8$, Pr$=0.1$ and $y=0.5$ at $\tau=0.5$; –··–, Bo$=10^9$, Pr$=0.1$ and $y=0.5$ at $\tau=0.5$; ——·—, Bo$=10^6$, Pr$=0.01$ and $y=0.5$ at $\tau=1.0$; —— (bold), Bo$=5\times10^6$, Pr$=0.05$ and $y=0.5$ at $\tau=1.0$; $\cdots\cdots$ (bold), Bo$=5\times10^7$, Pr$=0.5$ and $y=0.5$ at $\tau=1.5$; —— (bold), Bo $=10^7$, Pr$=0.1$ and $y=0.3$ at $\tau=0.5$; –·– (bold), Bo$=10^7$, Pr$=0.1$ and $y=0.7$ at $\tau=1.0$; –··– (bold), Bo$=10^7$, Pr$=0.1$ and $y=0.9$ at $\tau=1.5$.

the start-up stage for the selected values of Bo, Pr, y, and τ. The numerical results presented in Fig. 20(a), where the horizontal vertical velocity profiles within the inner viscous boundary layer at the start-up stage are presented, and v and x are scaled by v_m and δ_{vi}, respectively, show that the scales v_m and δ_{vi} collapse all sets of data onto a single curve, indicating that the vertical velocity similarity is well preserved within the inner viscous boundary layer at the steady state, that is, the horizontal vertical velocity profile within the inner viscous boundary layer at the start-up stage can be expressed as follows

$$\frac{v}{v_m} = f\left(\frac{x}{\delta_{vi}}\right), \qquad (63)$$

where $f(x/\delta_{vi})$ represents some function of x/δ_{vi}. Figure 20(b), where the horizontal vertical velocity profiles within the outer viscous boundary layer at the start-up stage are presented, and v and $(x-\delta_{vi})$ are scaled by v_m and δ_T respectively, show that the scales v_m and δ_T satisfactorily collapse all sets of data onto a single curve, indicating that the vertical

velocity similarity is also well preserved within the outer viscous boundary layer at the start-up stage, that is, the horizontal vertical velocity profile within the outer viscous boundary layer at the start-up stage can be expressed as follows

$$\frac{v}{v_m} = f\left(\frac{x - \delta_{vi}}{\delta_T}\right), \tag{64}$$

where $f[(x - \delta_{vi})/\delta_T]$ represents some function of $(x - \delta_{vi})/\delta_T$.

V. CONCLUSIONS

A set of scalings have been derived to describe the basic features for the natural covection boundary layer flow adjacent to an evenly heated semi-infinite vertical plate with isoflux boundary condition. The scalings have been developed for fluids with Prandtl number less than 1.0 with the intention, in paticular, of determining the Prandtl number effect for such flows. The scalings have been validated and scaling constants obtained by comparison with numerical solutions obtained using an unsteady Navier-Stokes solver. The numerical solutions provide a full description of the flow behavior provided sufficiently fine grid and time-step are using to resolve all features of the flow.

Based on the scaling analysis it was hypothesized that the velocity boundary layer consisted of an inner and an outer region that would require separate scalings. In the inner region the behavior of the velocity is determined by a viscous bouyancy balance in the vertical momentum equation. In the outer region the velocity boundary layer will be governed by the behavior of the thermal boundary layer, as has been verified. The thermal boundary layer has been shown to obey a single similarity law, while two similarity regions exist for the velocity boundary layer, corresponding to the inner and outer regions developed in the scaling analysis.

It has also been shown that applicability of the scalings is limited by both distance from the plate origin and Boussinesq number, showing that close to the origin and/or at low Boussinesq numbers the flows are no longer self-similar, as expected. This result is also seen in the comparison between the DNS results and the solution of Sparrow and Greg [8], which is a similarity solution. From these results it can be seen that for agreement to within 1% it is necessary for the local Boussinesq number, that is the Boussinesq number based on plate location y, to be greater than approximately $10^6 Pr$. This behaviour is also seen in the camparison of the scaling relations and DNS results for varying y and Bo.

[1] Y. Jaluria, *Natural Convection Heat and Mass Transfer* (Pergamon, Oxford, 1980).

[2] B. Gebhart, Y. Jaluria, R. L. Mahajan, and B. Sammakia, *Buoyancy-Induced Flows and Transport* (Hemisphere, New York, 1988).

[3] J. M. Hyun, Adv. Heat Transfer **24**, 277 (1994).

[4] A. Bejan, *Convection Heat Transfer*, 3rd ed. (John Wiley & Sons, New York, 2004).

[5] R. J. Goldstein *et al.*, Int. J. Heat Mass Transfer **48**, 819 (2005).

[6] M. J. Stewart and F. Weinberg, J. Cryst. Growth **12**, 217 (1972); A. A. Mohamad and R. Viskanta, Int. J. Numer. Methods Fluids **13**, 61 (1991).

[7] H. Sammouda, A. Belghith, and C. Surry, Int. J. Numer. Methods Heat Fluid Flow **9**, 612 (1999).

[8] E. M. Sparrow and J. L. Gregg, Trans. ASME **78**, 435 (1956).

[9] H. K. Kuiken, J. Fluid Mech. **37**, 785 (1969).

[10] E. R. G. Eckert, *Introduction to the Transfer of Heat and Mass* (McGraw-Hill, New York, 1950).

[11] R. L. Mahajan and B. Gebhart, Int. J. Heat Mass Transfer **21**, 549 (1978).

[12] K. K. Park and V. P. Carey, Numer. Heat Transfer **8**, 317 (1985).

[13] Y. Joshi, Int. J. Heat Mass Transfer **30**, 2686 (1987).

[14] J. H. Merkin, J. Eng. Math. **19**, 189 (1985); J. H. Merkin, J. Eng. Math. **23**, 273 (1989); J. H. Merkin, I. Pop, and T. Mahmood, J. Eng. Math. **25**, 165 (1991).

[15] G. Ramanaiah and G. Malarvizhi, Waerme- Stoffuebertrag. **27**, 393 (1992).

[16] J. H. Merkin, Int. J. Heat Fluid Flow **15**, 392 (1994); A. Kay, H. K. Kuiken, and J. H. Merkin, J. Fluid Mech. **303**, 253 (1995).

[17] J. S. Park and J. M. Hyun, Int. J. Heat Mass Transfer **41**, 4393 (1998); J. Fluid Mech. **451**, 295 (2002).

[18] A. J. Chamkha, Can. J. Phys. **80**, 1145 (2002).

[19] J. C. Patterson and J. Imberger, J. Fluid Mech. **100**, 65 (1980).

[20] A. Bejan, Int. J. Energy Res. **27**, 859 (2003).

[21] M. Jannot and T. Kunc, Int. J. Heat Mass Transfer **41**, 4327 (1998).

[22] K. H. Kim and J. M. Hyun, Numer. Heat Transfer, Part A **44**, 169 (2003).

[23] W. Lin, Ph.D. thesis, The University of Sydney, Sydney, 2000.

[24] W. Lin and S. W. Armfield, Int. J. Heat Mass Transfer **42**, 4117 (1999); Int. J. Heat Fluid Flow **22**, 72 (2001); Phys. Rev. E **69**, 056315 (2004); Int. J. Heat Mass Transfer **48**, 53 (2005).

[25] W. Lin, S. W. Armfield, and P. L. Morgan, Int. J. Heat Mass Transfer **45**, 451 (2002).

[26] C. Lei and J. C. Patterson, J. Fluid Mech. **460**, 181 (2002).

[27] W. W. Humphreys and J. R. Welty, AIChE J. **21**, 268 (1975).

[28] A. Bejan and J. L. Lage, J. Heat Transfer **112**, 787 (1990).

[29] D. Henry and M. Buffat, J. Fluid Mech. **374**, 145 (1998); A.

Juel, T. Mullin, H. B. Hadid, and D. Henry, J. Fluid Mech. **436**, 267 (2001).

[30] L.-G. Sundström and M. Vynnycky, J. Fluid Mech. **390**, 45 (1999).

[31] A. Yu. Gelfgat, P. Z. Bar-Yoseph, and A. Solan, J. Cryst. Growth **220**, 316 (2000).

[32] I. Di Piazza and M. Ciofalo, Int. J. Heat Mass Transfer **43**, 3027 (2000); S. Arcidiacono, I. Di Piazza, and M. Ciofalo, Int. J. Heat Mass Transfer **44**, 537 (2001); S. Arcidiacono and M. Ciofalo, Int. J. Heat Mass Transfer **44**, 3053 (2001).

[33] A. Shapiro and E. Fedorovich, J. Fluid Mech. **498**, 333 (2004); Int. J. Heat Mass Transfer **47**, 4911 (2004).

[34] B. P. Leonard, Comput. Methods Appl. Mech. Eng. **19**, 59

(1979).

[35] S. W. Armfield, Comput. Fluids **20**, 1 (1991); S. W. Armfield and R. L. Street, J. Comput. Phys. **153**, 660 (1999).

[36] S. W. Armfield and J. C. Patterson, J. Fluid Mech. **239**, 195 (1992).

[37] A. Hessamoddini, S. W. Armfield, and J. Imberger, Adv. Eng. Software **28**, 25 (1997).

[38] A. Javam, J. Imberger, and S. W. Armfield, J. Fluid Mech. **396**, 183 (1999).

[39] W. Lin and S. W. Armfield, Phys. Rev. E **66**, 066308 (2002); J. Fluid Mech. **403**, 67 (2000).

[40] M. P. Kirkpatrick, S. W. Armfield, A. R. Masri, and S. S. Ibrahim, Flow, Turbul. Combust. **70**, 1 (2003).